



# Experimental investigation and mathematical modelling of shale gas adsorption and desorption hysteresis

Jamiu M. Ekundayo<sup>a,b,\*</sup>, Reza Rezaee<sup>a</sup>, Chunyan Fan<sup>a</sup>

<sup>a</sup> Western Australian School of Mines: Minerals, Energy and Chemical Engineering, Curtin University, Australia

<sup>b</sup> State Key Laboratory of Oil and Gas Reservoir Geology and Exploitation, Southwest Petroleum University, Chengdu, Sichuan, 610500, China

## ARTICLE INFO

### Keywords:

Canning basin  
Ordovician goldwyer formation  
Pore saturation  
Sorption hysteresis  
TOC-Normalized clay  
Adsorbed phase density

## ABSTRACT

To quantify shale gas contents and hysteresis behaviour of the Ordovician Goldwyer shales as functions of temperature and rock properties, methane adsorption and desorption isotherms were measured at four temperatures. Early pore saturation was observed for all eight samples tested and consequently, the measured sorption isotherms could not be directly modelled by Langmuir isotherm or its modified version. Thus, a hybrid-modelling approach comprising the use of Dubinin–Radushkevich (D-R) model to obtain the adsorbed phase density ( $\rho_{ads}$ ) needed to convert excess amounts to absolute followed by Langmuir model to describe the resultant absolute isotherms. Significant hysteresis observed resulted in lower Langmuir parameters for the desorption isotherms compared to the adsorption isotherms. For both processes, Langmuir volumes positively correlated with TOC contents but showed no significant correlations with total clay contents. To capture the effect of clay contents, the ratio of total clay to TOC (subsequently referred to as clay-to-organic-carbon, COC) was applied as a single predictor instead. The results showed that Langmuir volumes, and the size of the hysteresis showed significant correlations with TOC contents and COC. Lastly, analytical models were developed for the temperature-dependence of Langmuir volume as functions of each of TOC contents and COC for both adsorption and for the first time, desorption isotherms. The models showed significant match with experimental results and as such, can be adopted for conditions beyond those investigated in this study.

## 1. Introduction

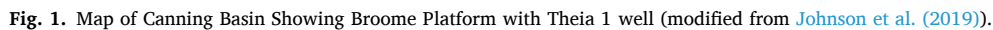
High-pressure adsorption of supercritical methane is often used to determine the gas contents of shale reservoirs at in situ conditions. This is because gas adsorption in the internal surface areas of the rock matrix is the primary storage mechanism in such reservoirs (Bell and Rakop, 1986; Curtis, 2002; King, 1993). The amount of gas adsorbed by a rock is affected by controllable factors such as pressure, temperature, and moisture contents (Bell and Rakop, 1986) as well as the rock's organic matter and mineral compositions. The relationship between the amount of gas adsorbed, at a constant temperature, and pressure is known as adsorption isotherm and can be measured experimentally using various techniques such as volumetric, spectroscopic, and gravimetric, among others. The measured adsorption is referred to as the excess adsorption which implies the difference in the amount of gas in the adsorbent at a given pressure and temperature and the amount that would otherwise be present as bulk phase if all the adsorbent's pore volume were accessible under the same conditions (Myers and Monson, 2014).

A typical workflow in determining the gas contents of shale resources involves the conversion of excess to absolute adsorption followed by a mathematical modelling of the resultant absolute adsorption isotherm, typically using the Langmuir model (Langmuir, 1918). Detailed discussions of the different types of adsorptions and how to convert from one to the other have been extensively discussed in the literature (Brandani et al., 2016; Myers and Monson, 2002, 2014). However, it is important to reiterate that the density of the adsorbed phase ( $\rho_{ads}$ ) controls the shape and size of the resultant absolute adsorption and consequently, the model parameters associated with the isotherm. Currently, there is no practical mechanism to measure  $\rho_{ads}$ . Thus, different approaches have been devised to estimate this parameter, including modifications to original adsorption models to handle supercritical conditions. Despite these efforts,  $\rho_{ads}$  remains an elusive parameter to estimate accurately.

The workflow described above is an indirect method used extensively for estimating gas contents in shale reservoirs and coal-seams. Several samples might be collected at different depths in a well to

\* Corresponding author. Western Australian School of Mines: Minerals, Energy and Chemical Engineering, Curtin University, Australia.

E-mail address: [jamiu.ekundayo@postgrad.curtin.edu.au](mailto:jamiu.ekundayo@postgrad.curtin.edu.au) (J.M. Ekundayo).



Just as gas adsorption is akin to reserves estimation in shale reservoirs, gas desorption is also paramount to gas transport (and hence, production) in such reservoirs (Ekundayo and Rezaee, 2019b; Wang et al., 2017a, b). The importance of gas adsorption and desorption processes in modelling flows in shale gas reservoirs has also been re-emphasized by two recent independent review articles (Taghaviinejad

et al., 2020; Yang and Liu, 2020). However, despite the significant records of gas adsorption studies in shale reservoirs, studies involving desorption of methane from shales at high-pressure and high-temperature conditions remain very scanty. It is generally believed that high-pressure methane adsorption in shale reservoirs is a physical and reversible process (Kierlik et al., 2002; Monson, 1983). Hence, the existence of sorption hysteresis under high-temperature, high-pressure conditions is often doped as an experimental error (Bell and Rakop, 1986; Dutta et al., 2011; Ozdemir, 2017). However, findings from studies involving methane-coal systems have refuted this argument, suggesting other factors unconnected with the experimental parameters, might be responsible for this phenomenon (Battistutta et al., 2010; Bell and Rakop, 1986; Bhowmik and Dutta, 2019; Busch et al., 2003; Dutta et al., 2011; Ekundayo and Rezaee, 2019c; Feng et al., 2016; Jessen et al., 2008; Liu et al., 2017b; Ozdemir, 2017; Wang et al., 2017a, b; Wei et al., 2017; Wei et al., 2013; Weishauptová et al., 2015; Zhang and Liu, 2016; Zhang et al., 2015). Excellent summaries of the key factors which researchers have identified as the primary causes of sorption hysteresis in supercritical methane-coal systems at high pressures are available in (Ekundayo et al., 2020; Ekundayo and Rezaee, 2019c; Wang et al., 2014).

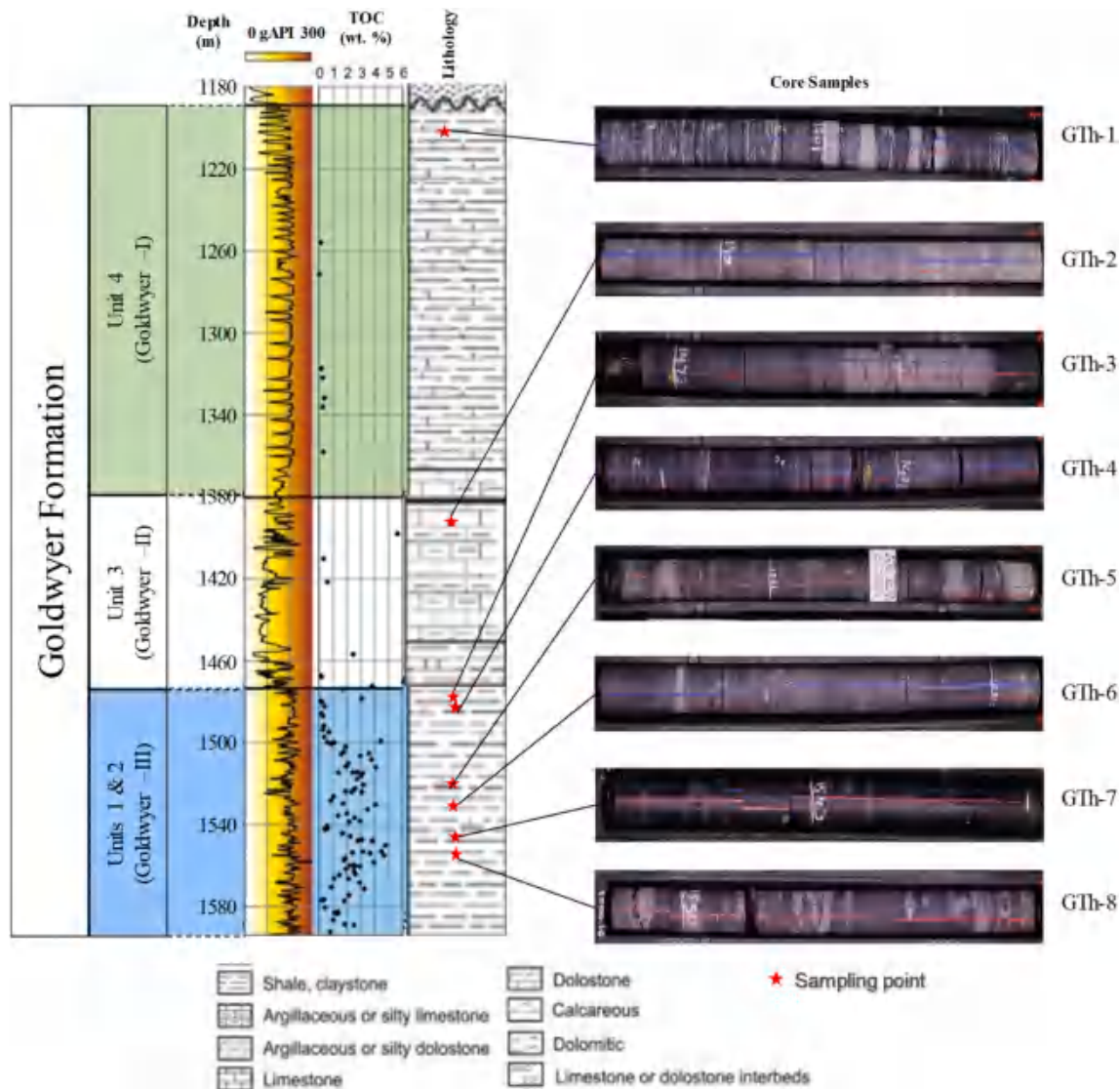


**Fig. 2.** Gamma-ray, TOC content and lithological distributions in Theia 1 well drilled into Broome Platform with core images of our study samples (modified from Spaak et al. (2017)).

In addition to the lack of enough studies on high-pressure methane desorption in shale formations, there is no record of an empirical model to estimate the Langmuir parameters for desorption. Also, the reported cases of high-pressure desorption of methane in shales and coals were either not modelled mathematically, or described using the Langmuir model with or without modifications. For example, while [Zhang and Liu \(2016\)](#) modelled desorption isotherms of methane in coals using Langmuir model multiplied by a factor referred to as the hysteretic factor, a parameter the authors introduced to define the fraction of the gas-adsorbed sites available for desorption, [Wei et al. \(2017\)](#) added a constant referred to as the residual adsorption capacity to Langmuir model to achieve the same objective for methane in shale. To avoid the subjectivity associated with these modifications, this study applies the Langmuir model without modifications (similar to [Bell and Rakop, 1986](#)). Besides the elimination of subjectivity, the use of the unmodified Langmuir model allows for an unbiased comparison of the model parameters for desorption isotherms with the corresponding values from adsorption isotherms. Furthermore, this study attempts to develop the first ever mathematical models to predict the Langmuir parameters for desorption of methane in shales as functions of both temperature and rock properties. Moreover, while the predictive models will be based on Goldwyer shales, the approach used can be replicated in other shale

formations especially those with clay (illite/mica) contents.

## 2. Geological overview

The shale samples used in this study were from the Ordovician Goldwyer Formation in the Broome Platform of the Canning Basin, Western Australia. As shown in [Fig. 1](#), the Broome Platform is one of the tectonic elements separating the two depocenters, namely the NW-SE Fitzroy trough – Gregory sub-basin and the south bound Willara and Kidson sub-basins, structurally compartmentalizing the Canning Basin ([Hashimoto et al., 2018](#); [Kennard et al., 1994](#); [Parra-Garcia et al., 2014](#)). The Goldwyer Formation occurs within the Ordovician-Silurian sequence and are predominantly made up of oil and gas-prone kerogen types II & III ([Bahar and Triche, 2013](#)). The Goldwyer Formation was deposited in open to intertidal marine environment during the maximum transgressive systems tract ([Delle Piane et al., 2015](#); [Haines, 2004](#); [Kennard et al., 1994](#); [Zhen et al., 2020](#)). The Formation is primarily composed of alternating proportions of calcareous mudstone and dolomitized limestone with sparse distributions of pyrite mostly in the south-east area of the basin ([Alshakhs, 2017](#); [Zhen et al., 2020](#)). Structurally, the Goldwyer Formation is sub-divided into upper (Goldwyer – I), middle (Goldwyer – II) and lower (Goldwyer – III) with evidence



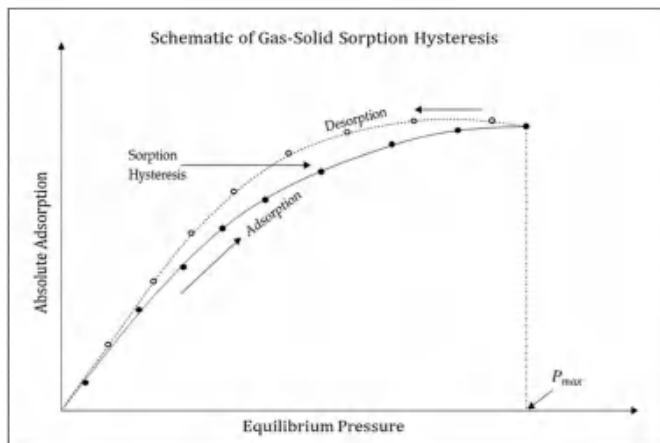


Fig. 3. Illustration of hysteresis between gas-solid adsorption and desorption isotherms.

showing vertical and areal variations in geochemical properties and source rock potential across the Formation (Johnson, 2019). Along the eastern part of the formation, the upper Goldwyer is reported to have excellent geochemical properties (Bahar and Triche, 2013; Cadman et al., 1993) and consequently, excellent hydrocarbon generating potential due to the abundance of *Gleocapsomorpha prisca* (*G. prisca*) (Spaak et al., 2017). Theia 1 well recently drilled on the Broome Platform has provided further information on the source rock potential of the lower Goldwyer Formation in this platform. Samples taken from the Theia 1 well showed evidences of good source rock potential in the lower Goldwyer Formation contrary to the previously held views that the formation is poorly developed in the northern of the sub-basin (Hashimoto et al., 2018; Kennard et al., 1994; Spaak et al., 2017).

In this study, eight shale samples were selected from the Theia 1 well to cover the different sub-divisions of the Goldwyer Formation as shown in Fig. 2. Core descriptions revealed that the shallowest sample, GTh-1 is predominantly claystone with traces of limestone while the rest of the samples contain varying proportions of (calcareous) mudstone and (fossiliferous) limestone. The core images also reveal evidences of thin laminations in the samples. This may also be a reason for the reported variations in properties both vertically and laterally (Johnson, 2019). Moreover, the middle Goldwyer appears to be richer in limestone while the lower Goldwyer unit contains higher proportion of mudstones with variable amounts of limestone. Evidences of post-depositional diagenetic changes such as quartz cementation, calcite cementation and dissolution, clay illitization and organic matter pyritization have been reported in the Goldwyer Formation (Delle Piane et al., 2015).

### 3. Sample and methods

#### 3.1. Sample characterization

The samples used in this study were selected from the Ordovician Goldwyer Formation in the Canning Basin, Western Australia. The samples were selected at different depths in the same well. Geochemical and mineralogical characterization of the samples were conducted using RockEval-6® pyrolysis and x-ray diffraction (XRD) techniques, respectively. Following the geochemical and mineralogical characterization, five of the samples were subjected to low-pressure nitrogen adsorption and desorption experiments to quantify their pore-size distributions and related pore-structure characterization. The choice of these five samples was dictated by sample availability. The nitrogen isotherms were measured at 77.3K and relative pressure ( $P/P_0$ ) range from about 0.01 to 1 for all five shale samples using Micromeritics® Tristar II 3020 apparatus. Prior to the tests, each sample was pulverized and sieved to particle sizes 44–74  $\mu\text{m}$  (325–200 mesh). This range was selected to cover a

wide range of pore sizes typically found in shales and more so, to provide adequate surface areas favourable to gas adsorption (Yan-Yan et al., 2016; Zou and Rezaee, 2016). An aliquot of each pulverized sample was then degassed at a temperature of 110 °C for at least 8 h followed by the adsorption and desorption measurements. The isotherms and their associated parameters (such as pore-size distributions, surface areas and pore volumes) were automatically generated by the equipment's inbuilt software system using the Brunauer-Emmett-Teller (BET) model (Brunauer et al., 1938) for isotherm fitting and density functional theory (DFT) (Lastoskie et al., 1993, 1997; Ustinov and Do, 2004, 2005) for pore size distribution (PSD).

#### 3.2. Measurement and modelling of methane sorption isotherms & hysteresis

Methane adsorption and desorption isotherms were measured at 25 °C, 40 °C, 60 °C and 80 °C for each sample using a high-pressure volumetric analyser (HPVA-II 200®). The equipment uses the volumetric technique to measure the sorption isotherms of a gas on powdered rock samples and helium expansion for void volume measurements. Details of the measurement procedures and volumetric calculations have been extensively discussed in the literature (Ekundayo and Rezaee, 2019a, 2019c; Zhang et al., 2015; Zou et al., 2017). Prior to helium calibration, an aliquot of each sample was degassed in a furnace under vacuum at 110 °C for at least 16 h to ensure all moisture contents and light hydrocarbons are completely removed. The measured excess isotherms ( $V_{exc}$ ) were converted to absolute isotherms ( $V_{abs}$ ) using equation (1) below:

$$V_{abs} = V_{exc} / \left( 1 - \frac{\rho_{bulk}}{\rho_{ads}} \right) \quad (1)$$

The bulk gas density ( $\rho_{bulk}$ ) was obtained from Soave's modified Benedict-Webb-Rubin's equation of state (SBWR-EOS) (Soave, 1999). The resultant absolute isotherms were then represented by the traditional two-parameter Langmuir model (Langmuir, 1918) as shown in equation (2).

$$V_{abs} = \frac{V_L P}{P + P_L} \quad (2)$$

For each sample, the Langmuir volume,  $V_L$  and Langmuir pressure,  $P_L$  were determined for both adsorption and desorption isotherms.

Equations (1) and (2) are often combined to a three-parameter Langmuir model for easy calculation of both the Langmuir parameters and adsorbed phase density ( $\rho_{ads}$ ). However, it has been reported that this approach can be inappropriate within the pressure ranges tested in this study (Ekundayo and Rezaee, 2019b; Zhang et al., 2016) or in a case where the excess adsorption reaches an early maximum (Gasparik et al., 2012). Moreover, the method of linearly fitting the plot of excess adsorption – bulk density post-saturation has also been shown to be subjective especially where the post-saturation data points are too few to justify the mathematical fit (Ekundayo and Rezaee, 2019b). On these bases, the modified Dubinin-Radushkevich (DR) (equation (3)) (Sakurovs et al., 2007) was employed in this study to fit the measured adsorption data and obtain the value of the adsorbed phase density for each sample at each temperature. The calculated adsorbed phase density was then used in equation (1) to convert both the adsorption and desorption isotherms to absolute isotherms which were later modelled by equation (2). This hybrid DR-Langmuir modelling approach combined the superiority of the DR-model in calculating the adsorbed phase density (Rexer et al., 2013) for the range of pressures used in this study with the simplicity of Langmuir model.

$$V_{exc} = V_0 \exp \left\{ -D * \left( \ln \left( \frac{\rho_{ads}}{\rho_{bulk}} \right) \right)^2 \right\} \left( 1 - \frac{\rho_{bulk}}{\rho_{ads}} \right) \quad (3)$$

$V_0$  in equation (3) is the maximum absolute adsorption while  $D$  is a

**Table 1**  
Geochemical properties and Mineral Composition of study samples.

Sample ID	Depth (m)	Geochemical Properties					Mineral Contents				
		TOC (wt %)	S1 (mg/g)	S2 (mg/g)	S3 (mg/g)	Tmax (°C)	Quartz (wt. %)	K-Feldspar (wt. %)	Carbonate <sup>b</sup> (wt. %)	Pyrite (wt. %)	Total Clay <sup>a</sup> (wt.%)
GTh-1	1201	0.28	0.04	1.1	0.49	442	15.68	2.23	2.11	1.44	76.58
GTh-2	1390	1.26	0.63	2.43	0.28	454	12.42	1.24	0.25	0.77	83.49
GTh-3	1473	3.20	2.12	7.55	0.51	454	17.39	1.78	0.42	2.59	74.28
GTh-4	1478	2.82	1.57	4.66	0.43	456	20.11	2.63	3.93	1.60	67.52
GTh-5	1521	2.76	1.63	3.5	0.63	430	27.11	1.49	29.11	2.17	37.10
GTh-6	1531	0.75	0.51	0.85	0.41	458	12.93	1.91	12.71	1.75	68.44
GTh-7	1543	3.86	1.86	4.12	0.73	435	9.14	2.74	12.11	2.42	72.47
GTh-8	1550	4.16	2.85	6.96	0.53	430	21.61	11.13	14.21	1.47	46.33

<sup>a</sup> Total clay = Kaolinite + illite/mica + chlorite.

<sup>b</sup> Carbonate = calcite + dolomite.

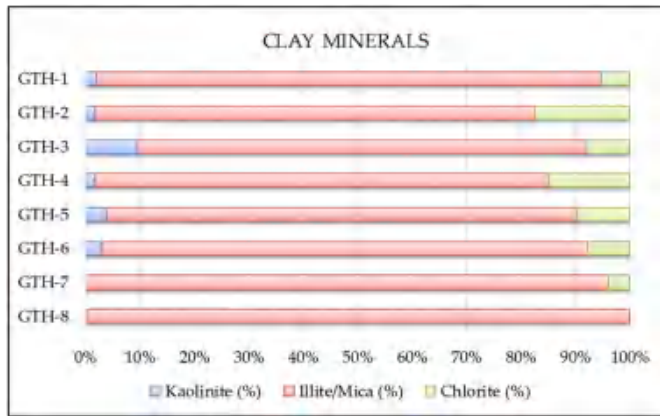


**Fig. 4.** Composition of total clay minerals in study samples.

parameter related to pore structure through the characteristic energy of adsorption ( $E$ ) (Hutson and Yang, 1997) as shown in equation (4) below.

$$D = \left( \frac{RT}{E_0 \beta} \right)^2 = \left( \frac{RT}{E} \right)^2 \quad (4)$$

Where  $E_0$  is the characteristic energy of adsorption for a reference vapour (typically benzene) and  $\beta$  is known as similarity constant (Hutson and Yang, 1997) which indicates the affinity of the adsorbent for the adsorbate (Tang et al., 2017). The characteristic energy of adsorption can be used to discriminate between physical adsorption (physisorption) and chemical adsorption (chemisorption) (Amrhar et al., 2015).

Following the calculations of the Langmuir parameters, the size of the observed hysteresis between the adsorption and desorption isotherms was quantified using both the areal hysteresis index ( $AHI$ ) (Zhang and Liu, 2016; Zhu and Selim, 2000) and improved hysteresis index ( $IHI$ ) (Wang et al., 2014) for each sample at each temperature. Fig. 3 is an illustration of a typical sorption hysteresis of supercritical methane on shale rocks.

The area covered by the hysteresis loop ( $A^{hys}$ ) is given as the difference between the areas bounded by desorption isotherm ( $A^{des}$ ) and adsorption isotherm ( $A^{ads}$ ) and can be expressed mathematically as:

$$A^{hys} = A^{des} - A^{ads} = \int_0^{P_{max}} \left( \frac{V_L^{des} P}{P_L^{des} + P} - \frac{V_L^{ads} P}{P_L^{ads} + P} \right) dP \quad (5)$$

The difference between  $AHI$  and  $IHI$  lies in the definition of the base area to which the hysteresis area is compared.  $AHI$  is the ratio of the hysteresis area to the area bounded to the pressure axis by the adsorption curve.

$$AHI = \frac{A^{hys}}{A^{ads}} = \frac{V_L^{des} \left( P_{max} - P_L^{des} \times \ln \left( \frac{P_L^{des} + P_{max}}{P_L^{des}} \right) \right)}{V_L^{ads} \left( P_{max} - P_L^{ads} \times \ln \left( \frac{P_L^{ads} + P_{max}}{P_L^{ads}} \right) \right)} - 1 \quad (6)$$

$IHI$  on the other hand, is the ratio of the hysteresis area to the area bounded to the adsorbed volume axis by the adsorption isotherm. The latter area is equivalent to the fully irreversible hysteresis area ( $A^{irr}$ ).

$$IHI = \frac{A^{hys}}{A^{irr}} = \frac{A^{hys}}{V_{max} * P_{max} - A^{ads}} \quad (7)$$

## 4. Results and discussion

### 4.1. Characteristics of study samples

Table 1 shows the results of the RockEval® pyrolysis and the key minerals from the XRD analysis. The samples have TOC contents in the range of 0.28–4.16 wt % covering a wide spectrum of qualities from poor to excellent based on the classification by Peters and Cassa (1994). The first peak,  $S_1$ , detected by the flame ionizing detector (FID) in the equipment (Lafarge et al., 1998; Peters, 1986) is in the range of 0.04–2.85 mg/g. This parameter represents the amount of hydrocarbon expelled at 300 °C prior to thermal cracking (Lafarge et al., 1998; Peters, 1986). The second peak,  $S_2$ , representing the amounts of hydrocarbon produced from the thermal cracking of the kerogen and heavy hydrocarbons present in the rock samples, is in the range of 0.85–7.55 mg/g. Similarly, the third peak,  $S_3$ , representing the amount of carbon dioxide produced through thermal cracking of kerogen at about 390 °C, is in the range of 0.28–0.73 mg/g.  $T_{max}$ , the temperature at which  $S_2$  was recorded ranged from 430 to 458 °C varied level of thermal maturity of the samples. Table 1 also shows that the samples exhibit a complex variation in mineral compositions. Six of the samples are composed primarily of clay minerals (ranging from 67.5% to 83.5%) while the remaining two samples (that is, GTh-5 and GTh-8) have lower clay contents, are slightly richer in quartz and more in carbonates. Combined with the quartz contents, the presence of potash-feldspar (K-feldspar) in all the samples indicates some, albeit varied degree of brittleness (Ma et al., 2019). However, the study of brittleness index (and similar geo-mechanical properties) is beyond the scope of this article.

As shown in Fig. 4, the samples are composed primarily of illite/mica with negligible to relatively small amounts of kaolinites and chlorites. This is consistent with the findings from (Delle Piane et al., 2015). Among other geological and depositional considerations, the abundance of the illite/mica in these shales can explain the low values of the TOC contents observed in this Formation. Illite can precipitate and block off small organic pores (Pevear, 1999) changing the rock textures and reducing the petrophysical properties of the samples (Delle Piane et al., 2015).

The results of the low-pressure nitrogen adsorption and desorption

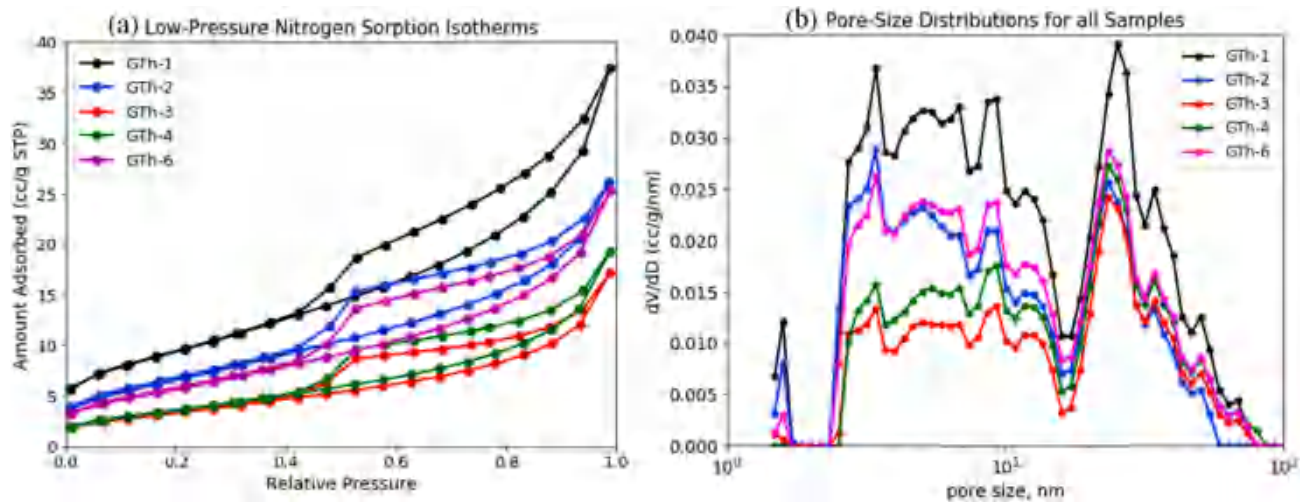


Fig. 5. Pore structure characterization using Low-pressure nitrogen adsorption.

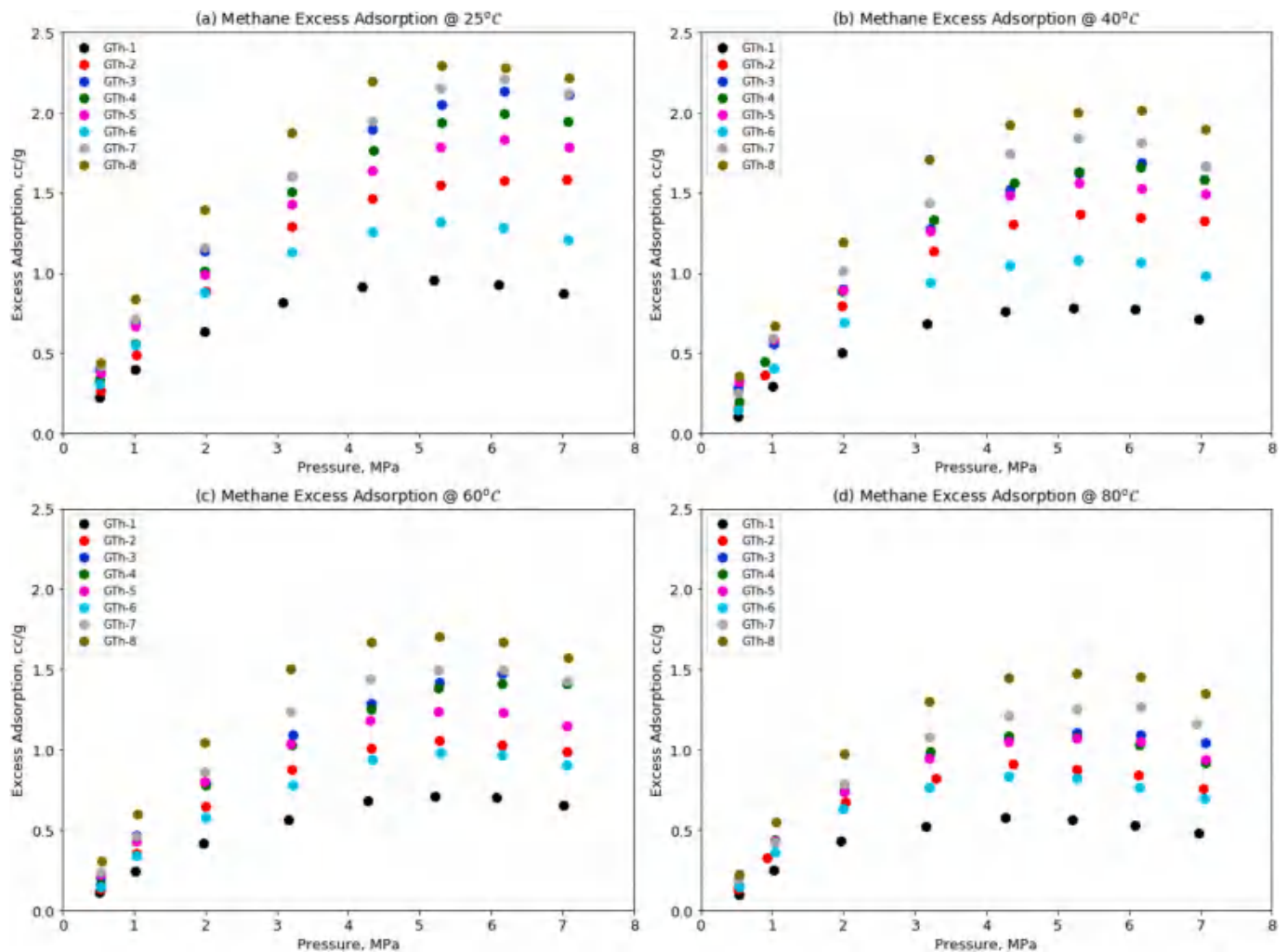


Fig. 6. Excess adsorption of methane on shale samples at different temperatures.

tests are shown in Fig. 5(a). Each sample exhibits adsorption isotherm that follows a monolayer-multilayer coverage up to relative pressure of about 0.8 beyond which the amount adsorbed sharply increases indicating capillary condensation (Jun-yi et al., 2014). Consequently, all five samples exhibit significant hysteresis of type H3 (IUPAC classification)

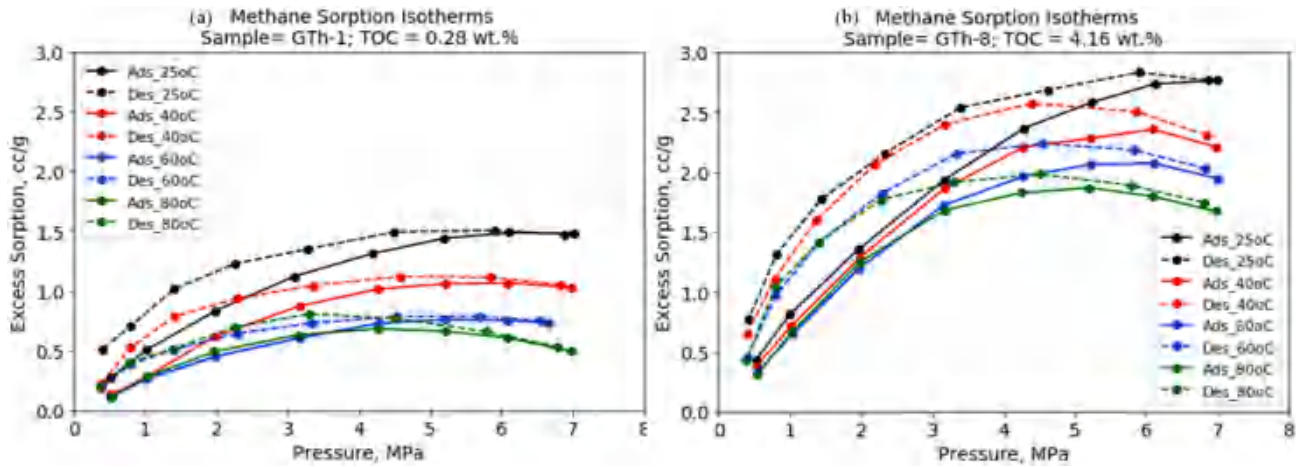
characterised by adsorption isotherms of type II and lower closures of the hysteresis loops, at relative pressure of about 0.4–0.5, which is an indication of the presence of slit-like nanopores (Thommes et al., 2015).

Fig. 5(b) shows the samples' PSDs based on the results of the low-pressure nitrogen experiments in combination with DFT slit-pore

**Table 2**

Relationships between maximum excess adsorption and rock properties.

T, °C	Maximum $V_{exc}$ vs TOC Content		Maximum $V_{exc}$ vs Total Clay		Maximum $V_{exc}$ vs COC	
	Equation	R <sup>2</sup>	Equation	R <sup>2</sup>	Equation	R <sup>2</sup>
25	$0.3173 \times \text{TOC} + 1.0304$	0.9517	$2.4921 - 0.0108 \times \text{Clay}$	0.1300	$2.0913 - 0.0047 \times \text{COC}$	0.7745
40	$0.2731 \times \text{TOC} + 0.8463$	0.9482	$2.1997 - 0.0107 \times \text{Clay}$	0.1733	$1.7592 - 0.0040 \times \text{COC}$	0.7692
60	$0.2191 \times \text{TOC} + 0.7347$	0.9443	$1.8074 - 0.0084 \times \text{Clay}$	0.1646	$1.4597 - 0.0031 \times \text{COC}$	0.7124
80	$0.1800 \times \text{TOC} + 0.6107$	0.9126	$1.6061 - 0.0087 \times \text{Clay}$	0.2499	$1.2084 - 0.0026 \times \text{COC}$	0.7077

**Fig. 7.** Shale gas adsorption and desorption isotherms and their associated hysteresis.**Table 3**

DR's model parameters at different temperatures.

Sample ID	Temp. = 25 °C			Temp. = 40 °C			Temp. = 60 °C			Temp. = 80 °C		
	$V_o$ , cc/g	$D$ (-)	$\rho_{ads}$ , kg/m <sup>3</sup>	$V_o$ , cc/g	$D$ (-)	$\rho_{ads}$ , kg/m <sup>3</sup>	$V_o$ , cc/g	$D$ (-)	$\rho_{ads}$ , kg/m <sup>3</sup>	$V_o$ , cc/g	$D$ (-)	$\rho_{ads}$ , kg/m <sup>3</sup>
GTH-1	1.65	0.15	136.90	1.49	0.20	106.67	1.31	0.19	112.61	1.11	0.21	75.95
GTH-2	2.89	0.17	164.07	2.53	0.18	133.60	2.01	0.21	105.04	1.68	0.19	82.68
GTH-3	3.73	0.13	240.54	3.00	0.15	193.42	2.64	0.16	158.72	2.00	0.17	106.96
GTH-4	3.60	0.16	188.07	3.04	0.18	142.58	2.62	0.17	160.23	2.15	0.23	78.24
GTH-5	3.12	0.12	230.34	2.73	0.15	152.24	2.30	0.19	110.26	1.99	0.19	90.40
GTH-6	2.25	0.15	139.85	2.06	0.21	107.99	1.80	0.19	114.19	1.62	0.22	76.62
GTH-7	3.84	0.14	224.72	3.44	0.21	119.64	2.87	0.21	110.45	2.42	0.21	94.65
GTH-8	4.08	0.16	157.09	3.76	0.19	122.57	3.26	0.21	100.62	2.86	0.21	89.97

**Table 4**Relationships between DR's maximum absolute adsorption ( $V_o$ ) and sample properties.

T, °C	$V_o$ vs TOC Content		$V_o$ vs Total Clay		$V_o$ vs COC	
	Equation	R <sup>2</sup>	Equation	R <sup>2</sup>	Equation	R <sup>2</sup>
25	$0.5615 \times \text{TOC} + 1.8054$	0.9245	$4.2708 - 0.0172 \times \text{Clay}$	0.1029	$3.6872 - 0.0084 \times \text{COC}$	0.7637
40	$0.4875 \times \text{TOC} + 1.5931$	0.9296	$3.9220 - 0.0178 \times \text{Clay}$	0.1471	$3.2146 - 0.0071 \times \text{COC}$	0.7278
60	$0.4213 \times \text{TOC} + 1.3461$	0.9453	$3.4199 - 0.0163 \times \text{Clay}$	0.1683	$2.7349 - 0.0059 \times \text{COC}$	0.6944
80	$0.3447 \times \text{TOC} + 1.1565$	0.8838	$3.0882 - 0.0169 \times \text{Clay}$	0.2534	$2.2939 - 0.0049 \times \text{COC}$	0.6546

kernels. As shown, the pores are (approximately) bi-modally distributed with average dominant pore sizes 4 nm and 25 nm. The Figure also shows small peaks in the PSDs below the 2 nm micropore boundary and minimal presence of macropores. This implies that mesopores (pore sizes from 2 nm to 50 nm) accounts for majority of the pores in all the samples. The negligible volume of micropores observed here may be due to limited accessibility of these small pores by nitrogen molecules as a result of pore blockage caused by illite precipitation (Delle Piane et al., 2015; Pevear, 1999) and other diagenetic reactions (Delle Piane et al., 2015).

It would be observed from Fig. 5 that the nitrogen uptakes (and consequently, the derived PSDs) are negatively correlated to TOC

contents. A similar finding has been reported by Guo et al. (2019) in clay-rich Longmaxi shale samples from the Sichuan Basin in China. While this is contrary to most published LPN2-GA results, it is in part due to the effect of the pore blockage by illite in the Goldwyer shales (as previously discussed). Nitrogen adsorption is believed to be controlled by the abundance of micropores and mesopores which are believed to be related to organic matters (Guo et al., 2019), hence the positive correlations found in the literature between nitrogen uptakes and TOC content. However, Goldwyer shales are clay-dominated and it has been reported that a larger portion of the mesopores are controlled by clay minerals (Yuan et al., 2019). Also, (most) clay minerals are polar and have strong affinity for polar molecules (such as nitrogen) (Thompson



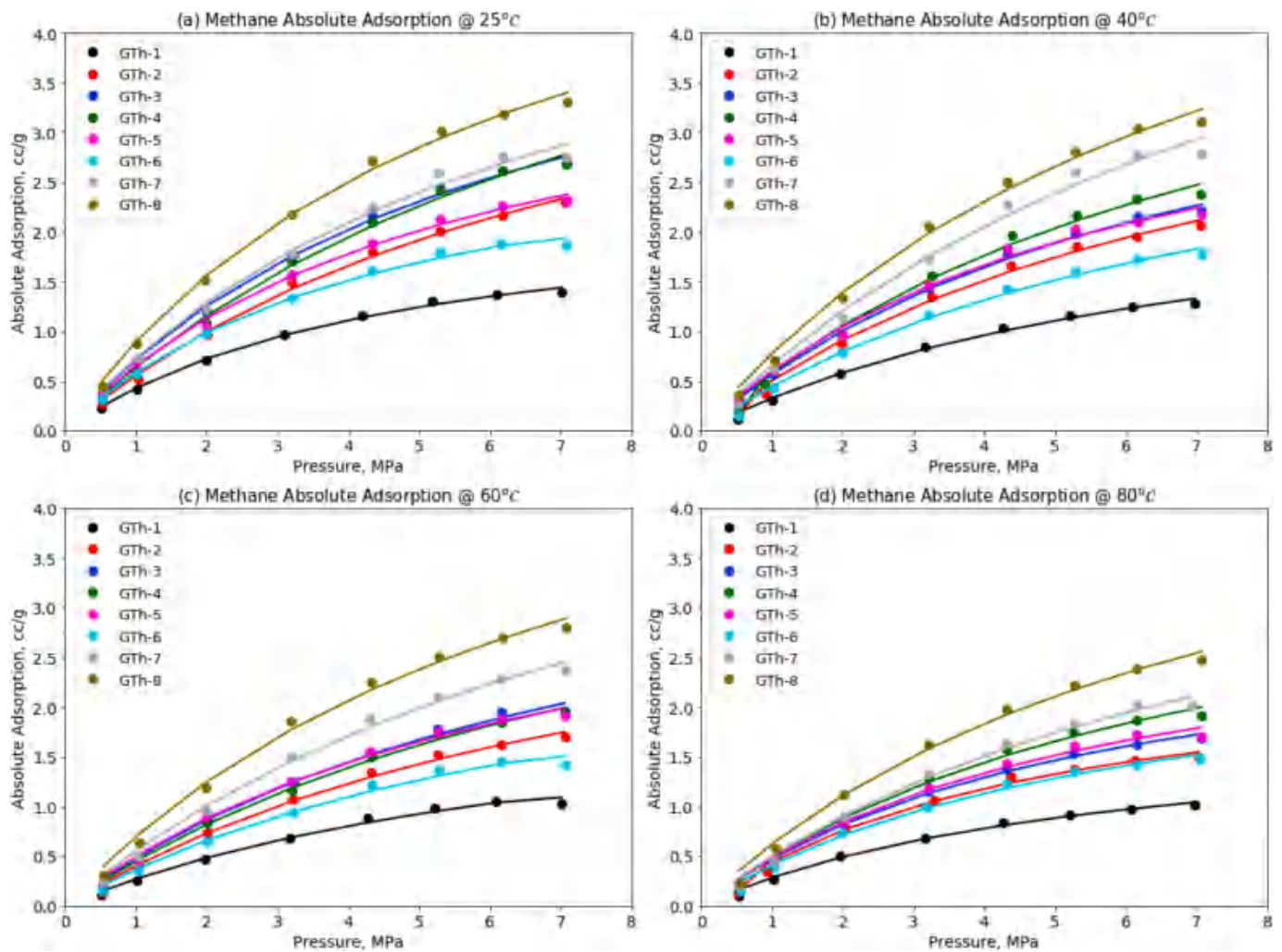


Fig. 8. Absolute adsorption isotherms of methane on shale samples (markers represent absolute adsorption while lines represent corresponding model fitting).

Table 5

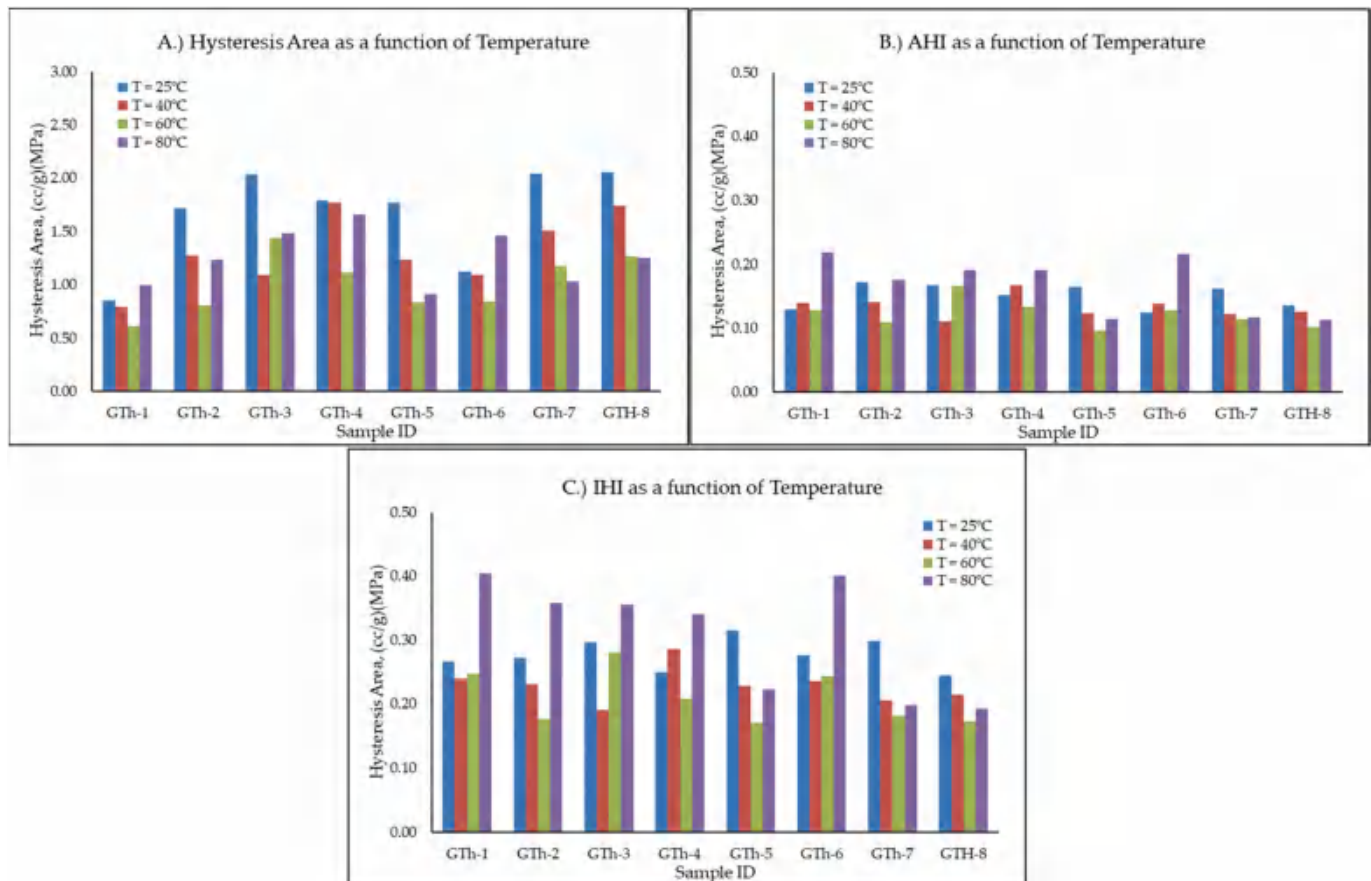
Langmuir model parameters for all samples at different temperatures.

Sample ID	Temperature = 25 °C						Temperature = 40 °C					
	Adsorption			Desorption			Adsorption			Desorption		
	$V_L$ , cc/g	$P_L$ , MPa	$R^2$	$V_L$ , cc/g	$P_L$ , MPa	$R^2$	$V_L$ , cc/g	$P_L$ , MPa	$R^2$	$V_L$ , cc/g	$P_L$ , MPa	$R^2$
GTH-1	2.37	4.54	0.9967	1.71	1.58	0.9915	2.73	7.36	0.9931	1.92	3.02	0.9957
GTH-2	5.00	8.02	0.9969	3.34	2.86	0.9922	6.79	10.17	0.9954	4.19	3.47	0.9946
GTH-3	5.22	6.31	0.9977	3.74	2.37	0.9984	4.53	7.00	0.9971	3.41	3.45	0.9986
GTH-4	6.23	8.79	0.9952	3.96	3.04	0.9977	5.30	7.99	0.9932	3.38	2.58	0.9964
GTH-5	4.18	5.37	0.9958	3.47	2.72	0.9927	4.11	5.84	0.9938	3.01	2.46	0.9957
GTH-6	3.22	4.52	0.9959	2.37	1.66	0.9948	3.80	7.55	0.9930	2.68	3.15	0.9951
GTH-7	5.59	6.66	0.9931	3.96	2.53	0.9963	6.83	9.30	0.9887	4.59	3.94	0.9984
GTH-8	6.31	6.07	0.9970	4.41	2.24	0.9969	6.77	7.73	0.9942	4.72	3.27	0.9969

Sample ID	Temperature = 60 °C						Temp = 80 °C					
	Adsorption			Desorption			Adsorption			Desorption		
	$V_L$ , cc/g	$P_L$ , MPa	$R^2$	$V_L$ , cc/g	$P_L$ , MPa	$R^2$	$V_L$ , cc/g	$P_L$ , MPa	$R^2$	$V_L$ , cc/g	$P_L$ , MPa	$R^2$
GTH-1	2.36	7.73	0.9909	1.50	2.64	0.9969	1.88	5.63	0.9920	1.50	2.38	0.9814
GTH-2	3.90	8.65	0.9929	2.72	3.94	0.9991	2.63	4.89	0.9928	2.37	2.87	0.9881
GTH-3	4.39	8.11	0.9944	2.96	3.02	0.9960	3.09	5.55	0.9968	2.19	1.76	0.9920
GTH-4	4.61	9.24	0.9950	3.45	4.71	0.9961	4.01	7.10	0.9901	2.76	2.45	0.9929
GTH-5	3.94	6.93	0.9941	2.98	3.53	0.9987	3.24	5.69	0.9924	2.45	2.61	0.9974
GTH-6	3.28	7.95	0.9907	2.10	2.78	0.9969	2.78	5.79	0.9918	2.23	2.51	0.9805
GTH-7	5.68	9.26	0.9932	3.61	3.55	0.9983	4.60	8.21	0.9923	3.18	3.56	0.9963
GTH-8	6.02	7.65	0.9931	4.27	3.49	0.9971	5.25	7.46	0.9932	3.89	3.61	0.9953





**Fig. 9.** Effect of temperature on the size of the hysteresis loop measured by (A) hysteresis area (B) areal hysteresis index (AHI) and (C) improved hysteresis index (IHI).

and Goynes, 2012). Although nitrogen does not have dipole moments, it has an effective quadrupole moment (Buckingham et al., 1968) which explains why the columbic law is often included in the force-fields for molecular simulation of nitrogen (Coasne et al., 2010). It is therefore possible that the contributions of the clay minerals to nitrogen adsorption in these samples superseded that of the organic matters leading to the deviation from the commonly observed trends between nitrogen uptakes and TOC contents. Moreover, the samples have lower quantities of quartz and feldspar and are therefore prone to higher mechanical compaction which might reduce the pore spaces available to nitrogen (Guo et al., 2019).

#### 4.2. High-pressure methane sorption isotherms and hysteresis

Fig. 6 shows the measured methane adsorption isotherms for all the eight samples described in the preceding sections. For each sample, the excess adsorption followed the expected decreasing trend with temperature. The amount adsorbed increased rapidly with pressure until about 5 MPa, beyond which the rate of increase was significantly lower and for some samples, adsorbed amounts decreased beyond this pressure point. This behaviour is a typical characteristic of excess adsorption of supercritical fluids on solids (Do and Do, 2005).

At the point of inflection, the rates of change of the adsorbed and bulk phase densities with pressure are the same. This phase equilibrium (between the adsorbed and free phases) occurred, for most of our samples, at pressures in the neighbourhood of the critical pressure of methane (4.6 MPa). Although lower than most of the values published for pressures at maximum excess adsorption of methane on shale, similar values exist in literatures for a few samples. For example, the “Geverik” shale sample in Gasparik et al. (2012) showed significant

maximum excess adsorption at about 6 MPa while samples X2-4 and X3-1 in Zhou et al. (2018) showed maximum excess adsorptions between 5 MPa–10 MPa. While no explanation was offered for these observations in the latter, the Geverik’s case was attributed to the high proportion of organic microporosity due to the sample’s over-maturity (Gasparik et al., 2012). On the contrary, our samples are predominantly mid to late matured marine shales and are characterised by larger proportions of mesopores in the inorganic minerals. Thus, thermal maturity alone cannot explain the early pore saturation observed in this study. It is expected that the high clay (illite) contents in these samples will counteract the high methane adsorbing capacity of their organic matters by reducing the surface areas available to methane adsorption in the organic pores and consequently, leading to earlier pore saturation than expected.

It follows from the above discussion that the methane sorption processes in our samples are controlled by a combined effect of their organic and inorganic contents. To capture this interplay, we employed the ratio of clay-content to TOC content (subsequently referred to “clay to organic carbon, COC” defined by equation (8)) which was first introduced by Liu et al. (2008) and hitherto referred to as RCO. COC is introduced in this study to better account for the effect of clay contents on adsorption and desorption model parameters.

$$COC = \frac{\text{Total Clay Content}}{\text{TOC Content}} \quad (8)$$

Table 2 summarises the relationship between the maximum excess adsorption and each of TOC content, total clay content, and the clay-to-organic-carbon (COC) ratio. These results show that maximum excess adsorption has a strong positive linear correlation with TOC content but a weak negative linear correlation with total clay contents. The opposing

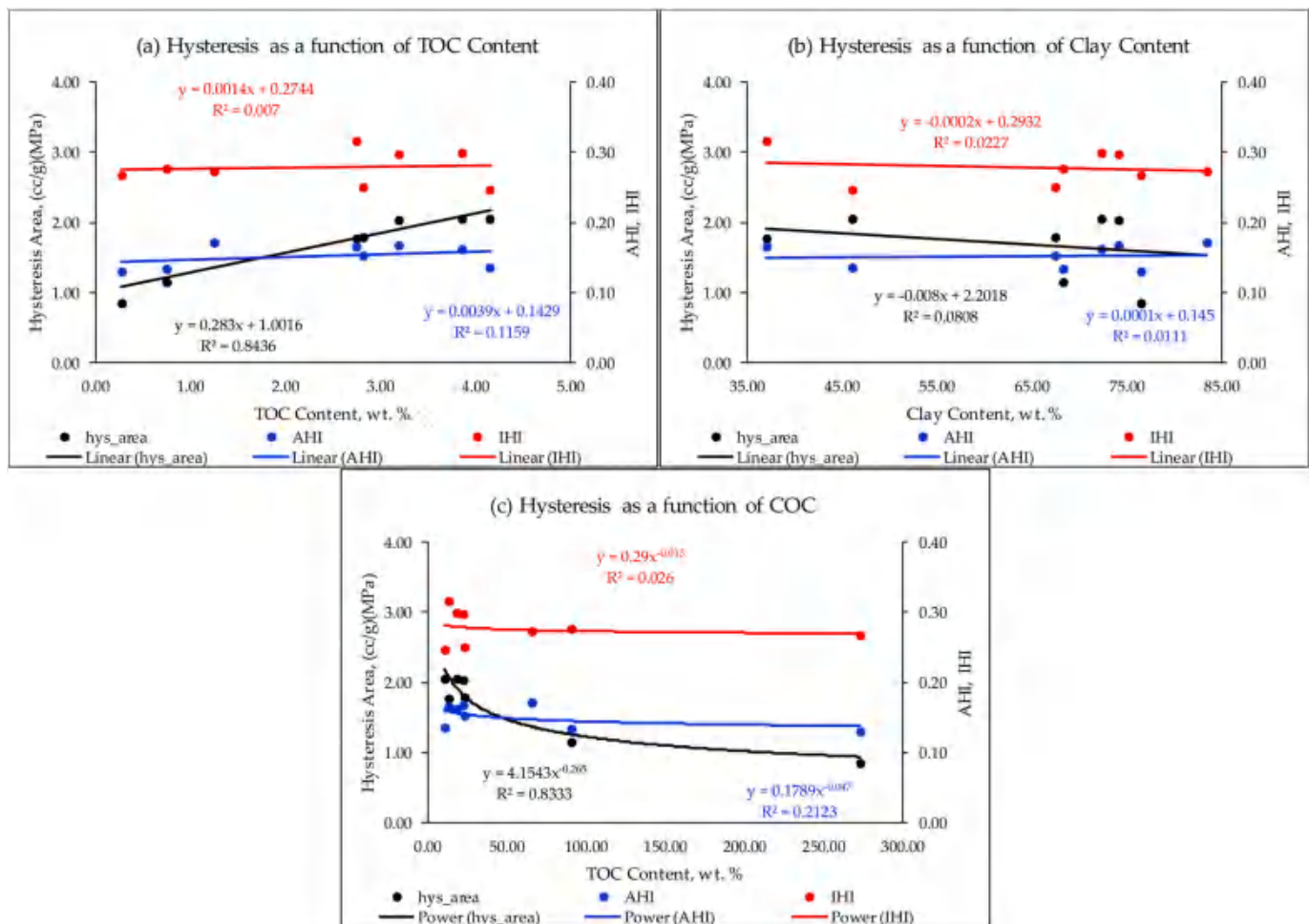


Fig. 10. Relationship between the sorption hysteresis at 25 °C and rock properties.

correlations of maximum excess adsorption with TOC and total clay contents support our explanation for the observed low excess adsorptions and early pore saturation. At each temperature, maximum excess adsorption shows positive correlations with COC with coefficients of determination ( $R^2$  values) greater than 70%, lower than those of correlations with TOC contents because of the influence of the clay contents. The decreasing slope and (vertical) intercept for each rock property is a reflection of the negative effect of temperature on adsorption.

In addition to the adsorption isotherms, desorption isotherms were measured at each temperature for each of the samples to enable us to examine the existence and size of sorption hysteresis and its relationships with rock properties. As shown in Fig. 7, significant hysteresis was observed between the adsorption and desorption isotherms at all test temperatures (kindly see Figure A1, appendix A, for the plots for all the samples). We have previously reported that the observed hysteresis was primarily due to the choice of equation of state (EOS) used to calculate the gas compressibility factors for experimental data analysis (Ekundayo and Rezaee, 2019b, 2019c).

#### 4.3. Isotherm modelling – model parameters & relationships with rock properties

As previously stated, the three-parameter Langmuir model was found to be inappropriate for isotherms exhibiting early excess adsorption maxima. Thus, the DR-model was used to parameterise the excess adsorption isotherms in this study. The value of  $\rho_{ads}$  obtained by fitting the modified DR-model to each adsorption isotherm was used to convert

both excess adsorption and (the corresponding) desorption isotherms to absolute sorption isotherms. The results of the modified DR-model fit to the adsorption isotherms are summarised in Table 3. The maximum absolute adsorption ( $V_0$ ) decreases with temperature in line with the expected negative effect of temperature on adsorption. However, contrary to the traditional practice of neglecting the temperature-dependence of the parameter  $D$  in the DR-model, the results here show that the values of  $D$  show positive, albeit weak to strong, correlations with temperature. This is also obvious from equation (4), which expresses the parameter  $D$  as a function of temperature. The characteristic energy of adsorption,  $E$  (not shown in the table) calculated from these results (using equation (4)) ranged from 5.7 to 7.2 kJ/mol indicating the adsorption type is physisorption (Amrhar et al., 2015). Adsorbed phase densities show mild to strong negative correlations with temperature for all samples except GTh-1 and GTh-6. Lastly, while no appreciable correlation with TOC content, total clay content or COC could be established for the parameter  $D$ , the characteristic energy ( $E$ ) of adsorption and the adsorbed phase density, the maximum absolute adsorption ( $V_0$ ) showed strong positive correlations with TOC content and COC but relatively no correlation with the total clay content as summarised in Table 4.

To take advantage of the greater popularity and commercial software implementations of the traditional Langmuir model, the resultant absolute sorption isotherms were described with the two-parameter Langmuir model represented by equation (2). Fig. 8 shows the calculated absolute adsorption isotherms (markers) and the corresponding Langmuir model fits (solid lines). The absolute adsorption isotherms at each temperature followed the expected positive trend with TOC

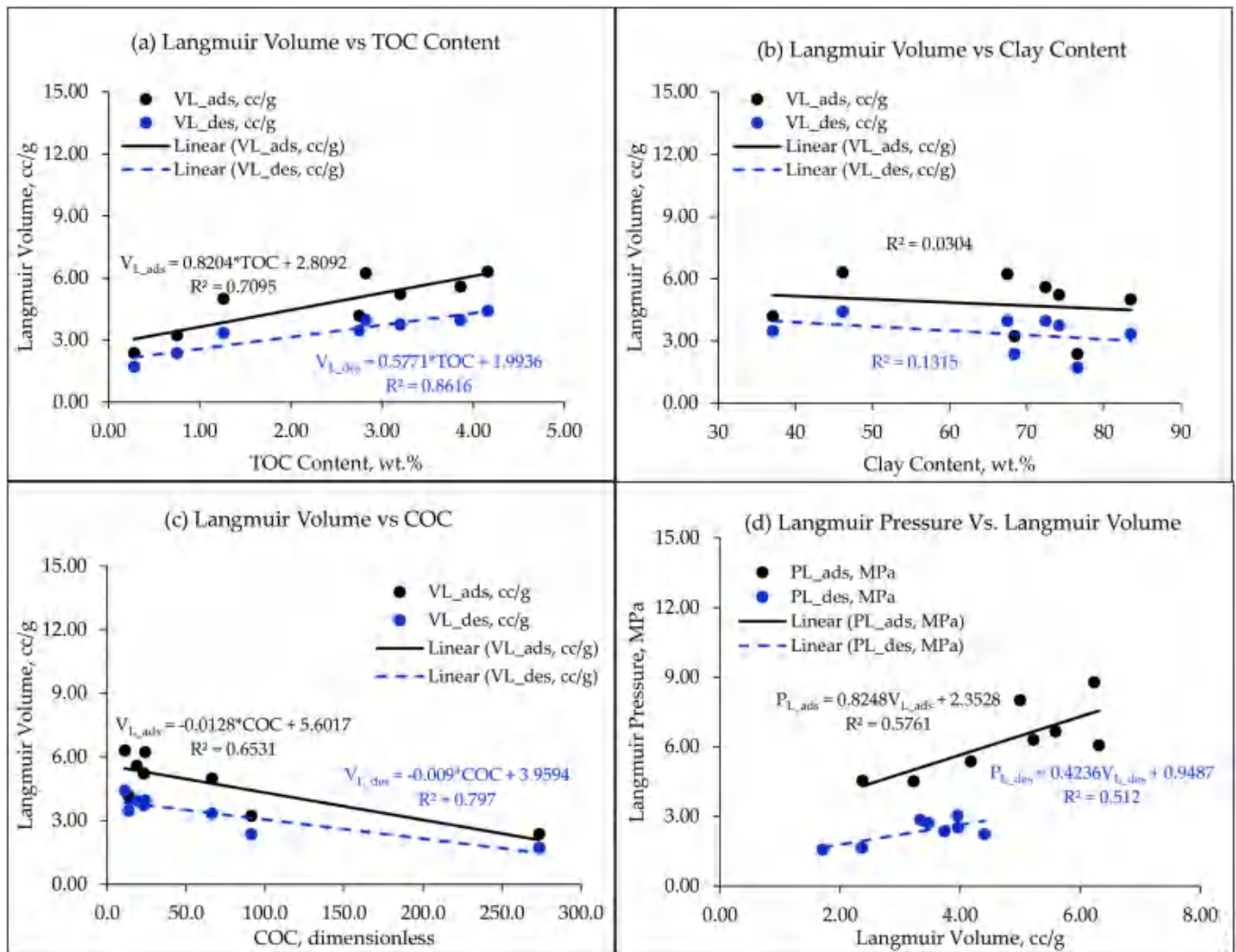


Fig. 11. Relationship between Langmuir volumes and TOC contents at 25 °C.

contents, with GTh-8 having the highest and GTh-1 having the lowest absolute adsorption at all temperatures. The values of the Langmuir volume and Langmuir pressure, for each sample and for each temperature, are summarised in Table 5. The results show that the Langmuir model adequately described the absolute adsorption and desorption isotherms with coefficients of determination ( $R^2$ ) exceeding 98%. Thus, it can be concluded that the Langmuir model, without any modification, can satisfactorily describe desorption isotherms. Due to the hysteresis, the desorption isotherms resulted in lower Langmuir volumes and pressures than the corresponding values obtained with the adsorption counterparts.

#### 4.3.1. Hysteresis quantifiers and relationship with temperature and rock properties

The size of each hysteresis loop, quantified by the indices given by equations (5)–(7), is significantly affected by temperature as shown in Fig. 9. As shown in Fig. 9(a), the size of the hysteresis loop, as well as the two other hysteresis indices, shrinks with increasing temperature, with some deviations at 80 °C. This observation is related to the thermodynamics of adsorption and desorption processes which is governed by the Gibb's free energy change ( $\Delta G$ ) given by equation (9) below:

$$\Delta G = -RT \ln K \quad (9)$$

Negative  $\Delta G$  is required for adsorption to be spontaneous and the more negative the value of  $\Delta G$ , the more favourable the adsorption is

(Zhang et al., 2016). Typically,  $\Delta G$  becomes less negative as temperature increases due to the inverse relationship between  $\ln K$  (where  $K$  = adsorption equilibrium constant) and temperature,  $T$  (Rani and Sud, 2015; Zhang et al., 2016). Consequently, adsorption is less spontaneous and the degree of freedom (randomness) of methane molecules increases (Rani and Sud, 2015). Thus, desorption is more favoured at higher temperature. For most of the samples, the observed hysteresis at 80 °C appeared to be characterised by methane readsorption (Ozdemir, 2004) causing unduly higher areas enclosed by the desorption isotherms. The higher values of the quantifying parameters are in part due to this phenomenon. Also, the lower values of adsorbed phase density at this temperature resulted in larger values of Langmuir volumes for the desorption process and consequently, larger hysteresis areas and hysteresis indices. Moreover, the choice of equation of state alone may not be a sufficient reason for the extent of the hysteresis. If we accept the validity of the principle of irreversible structural changes to the solid due to sorption processes (Liu et al., 2017b; Zhang and Liu, 2016), it may be possible to explain why the size of the hysteresis loop increased with temperatures (from 40 °C to 80 °C) for sample GTh-3. Adsorption has been reported to induce swelling in rock samples (Liu et al., 2017b; Zhang and Liu, 2016) and the swelling was said to be irreversible by the desorption-induced shrinkage (Cui et al., 2007). Thus, it can be hypothetically stated that the rate of adsorption-induced swelling in this sample increased with temperature. Thus, at higher temperatures, the sample swells more leading to reduced pore throats, increased



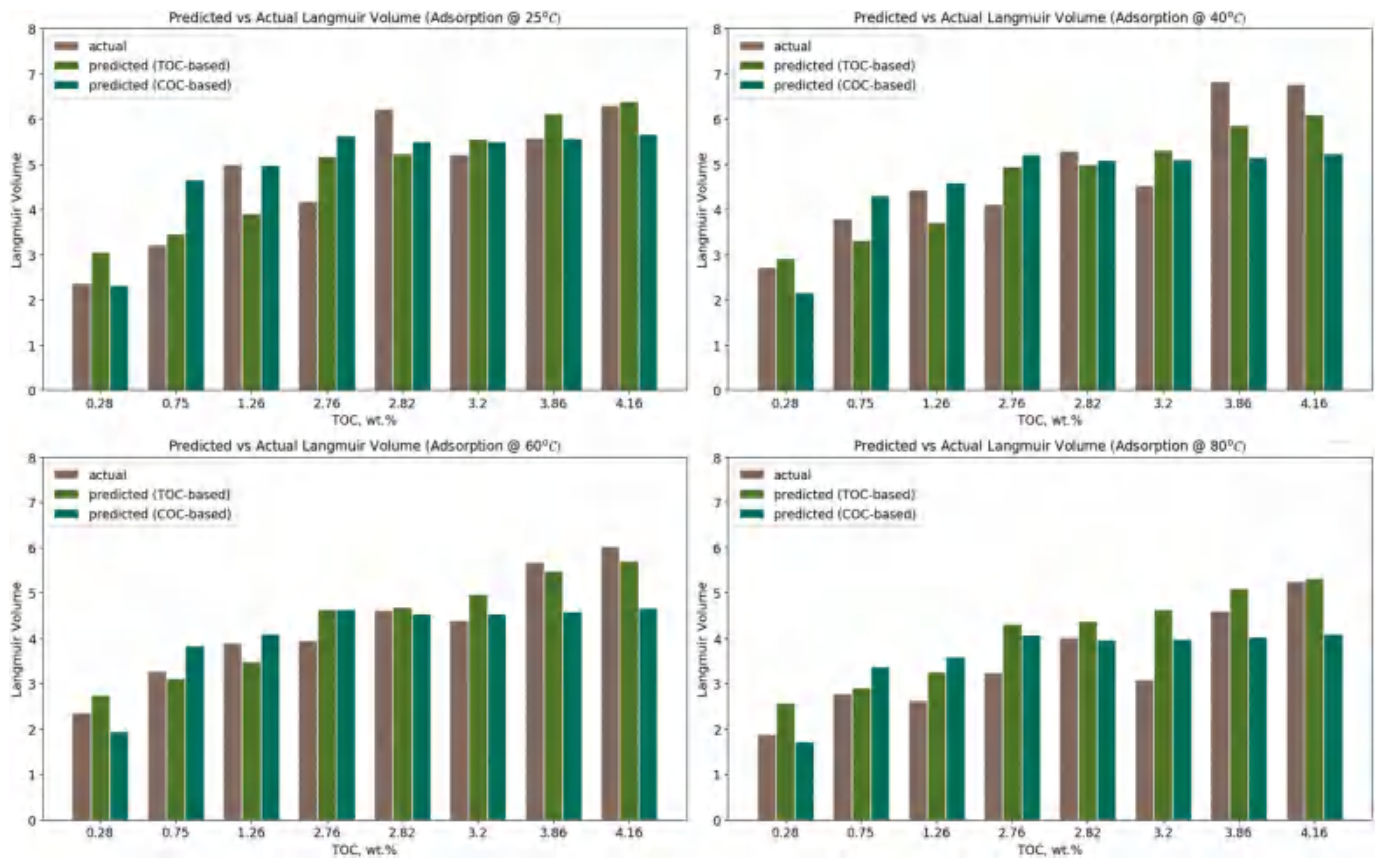


Fig. 12. Comparing predicted and actual Langmuir volumes for adsorption isotherms at 25 °C and 80 °C.

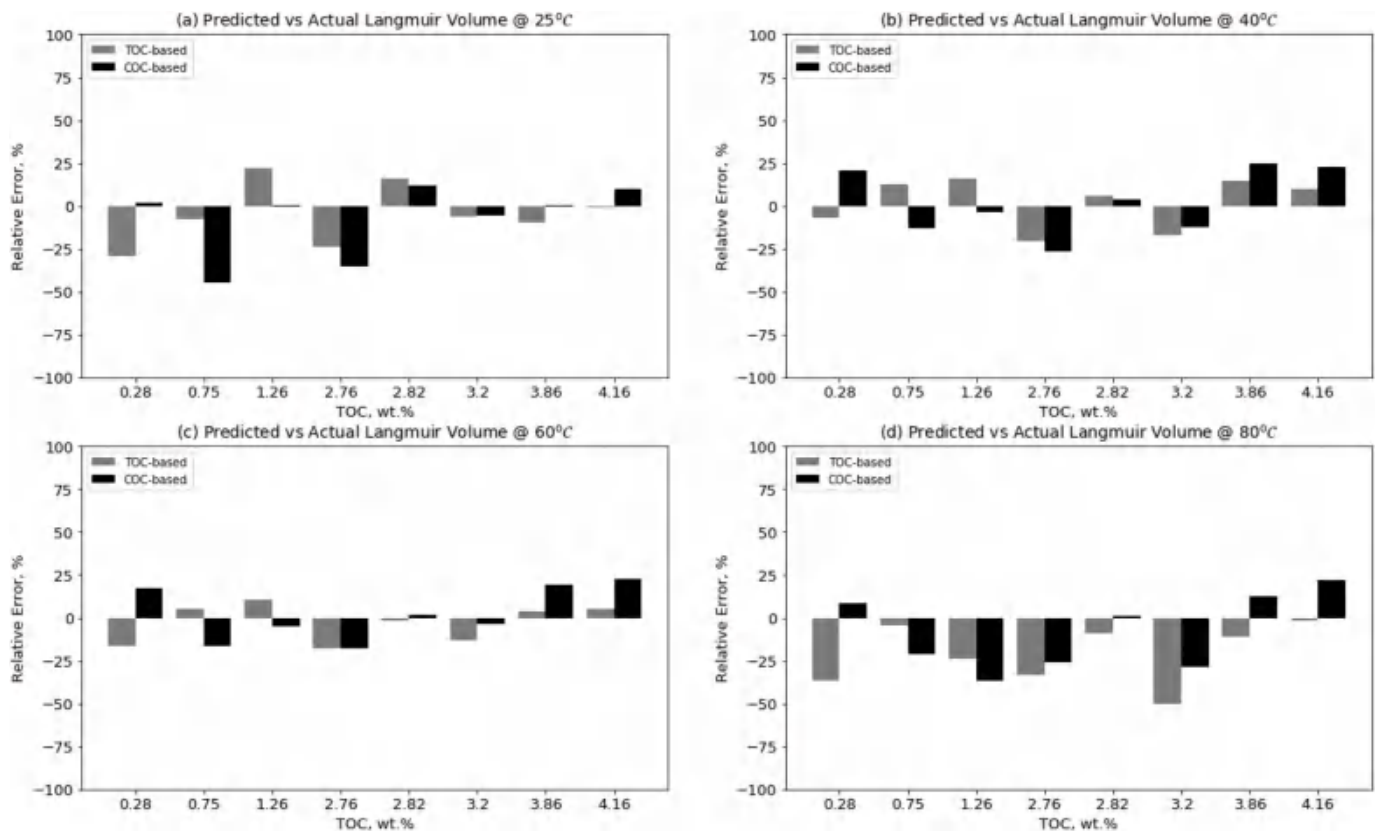


Fig. 13. Comparing the relative errors in calculated Langmuir volumes for adsorption isotherms.

**Table 6**

Coefficients of the quadratic relationship between temperature and each of  $m_1$  and  $c_1$ .

Process	$a_0$	$a_1$	$a_2$	$b_0$	$b_1$	$b_2$
Adsorption	0.0008	-0.0879	2.5212	-0.0057	0.6213	-9.7478
Desorption	0.0003	-0.0230	0.8049	-0.0019	0.1939	-2.6734

inaccessibility of pores, and consequently, increased gas trapping (Goodman et al., 2004; Wang et al., 2017a, b).

A comparison of the hysteresis quantifying parameters as functions of the rock properties is shown in Fig. 10. It is obvious that both AHI and IHI showed weak to negligible correlations with each of the three rock properties examined. Considering that the amounts adsorbed are different at different temperatures, it is expected that while the size of the hysteretic area may become smaller with increased temperature, the adsorption area also becomes smaller potentially leading to a higher ratio than expected. Thus, a comparison of the absolute values of areas enclosed by the hysteresis loop at different conditions offered better insights into the relationship between the size of sorption hysteresis and controlling factors like temperature and rock properties.

#### 4.3.2. Relationships between Langmuir parameters and shale properties

As shown in Fig. 11(a), Langmuir volumes for both adsorption and desorption processes showed strong positive correlations with TOC content, indicating that TOC content is the primary factor affecting adsorption and desorption in the Goldwyer Formation shales. A similar relationship between Langmuir volume and TOC content for methane adsorption has been reported in the literature for this formation (Zou and Rezaee, 2019). The strong relationships between Langmuir volumes and TOC contents can be explained in terms of the stronger affinity of organic matters for methane as a non-polar adsorbate. It is believed that

when a non-polar adsorbate (such as methane) binds with the hydrophobic organic matter of the adsorbent, the interfacial area between the non-polar adsorbate and the hydrophilic minerals (such as clay) is reduced (Thompson and Goynes, 2012). This observation is supported by the poor negative correlations found between Langmuir volumes and clay contents as shown in Fig. 11(b). However, in order not to downplay the contributions of the clay minerals to methane adsorption and desorption in the Goldwyer shales, COC was used as a predictor to capture the effect of clay contents on Langmuir volumes. As shown in Fig. 11(c), Langmuir volumes for both adsorption and desorption show significant correlations with COC at all test temperatures. The lower values of the correlation coefficients (for COC), compared to those of TOC content, are because of the poor correlations of Langmuir volumes with clay contents.

Langmuir pressures showed no appreciable correlation with either TOC, clay contents, or COC. However, positive (albeit weak to intermediate) linear correlations were observed between Langmuir pressures and Langmuir volumes as shown in Fig. 11(d). As shown in Figures A2–A5 (appendix A) similar trends (as the ones shown in Fig. 11) were observed at all test temperatures.

#### 4.3.3. Predictive models for Langmuir parameters

As shown in the example Fig. 11(a) (and Figure A2), Langmuir volumes for both adsorption and desorption isotherms follow linear relationships with TOC contents. If the slope and vertical intercept of this linear relationship at a given temperature are  $m$  and  $c$  respectively, then the following generalised equation can be written for the relationship between Langmuir volume and TOC content:

$$V_L = m \times \text{TOC} + c \quad (10)$$

Another observation from Figure A2 is that both the slopes and vertical intercepts are functions of temperature. Thus, for temperature  $T$

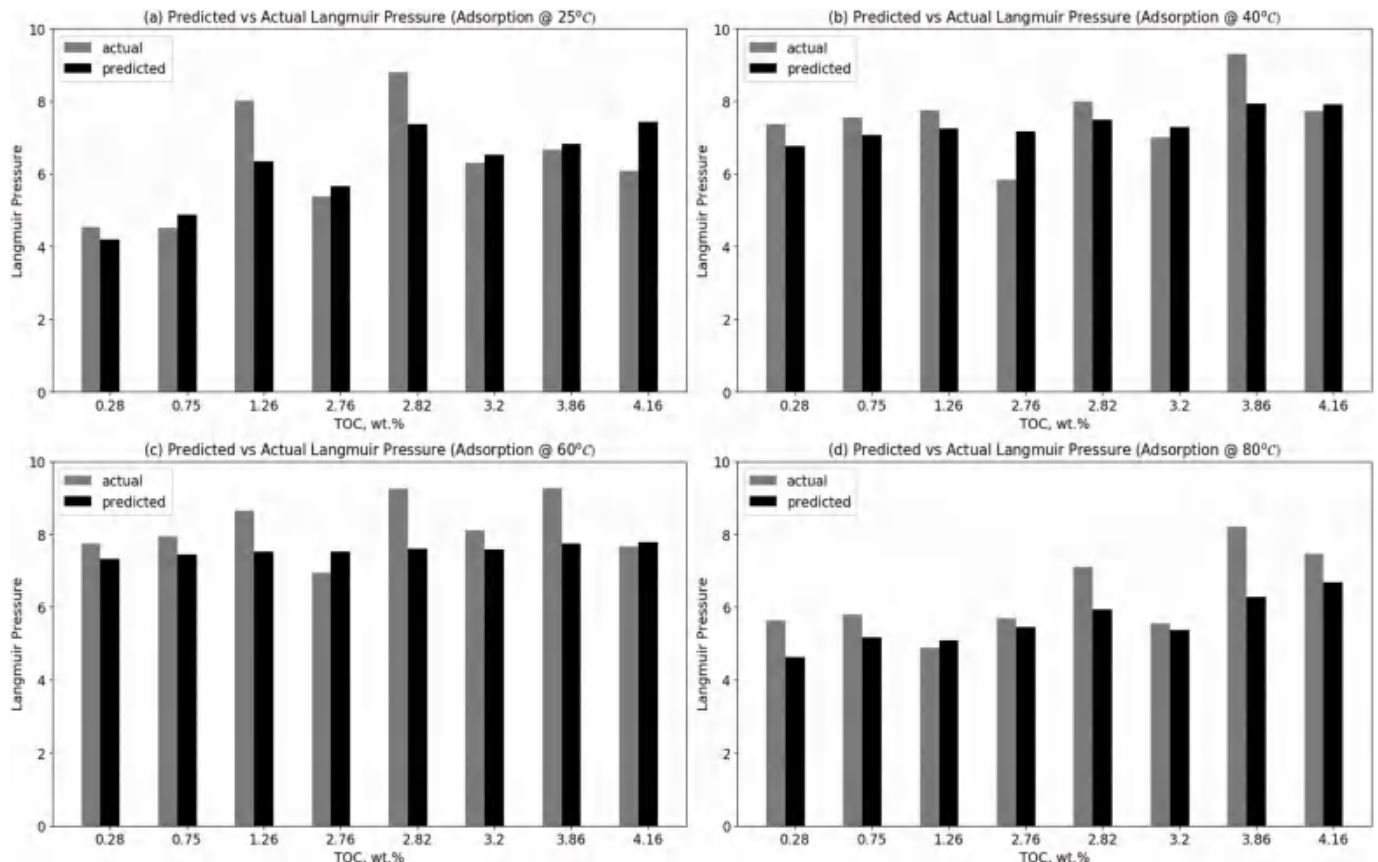


Fig. 14. Comparing predicted and actual Langmuir pressures at 25 °C and 80 °C.

in °C, the temperature-dependent nature of both  $m$  and  $c$  can be represented, for each the sorption process, by the following equations:

$$m_{ads}(T) = 0.9240 - 0.0027 \times T \quad (11a)$$

$$m_{des}(T) = 0.6861 - 0.0030 \times T \quad (11b)$$

$$c_{ads}(T) = 3.0199 - 0.0081 \times T \quad (12a)$$

$$c_{des}(T) = 2.2093 - 0.0083 \times T \quad (12b)$$

Combining equations (11) and (12) with equation (10), a single relationship was derived for the temperature-dependence of Langmuir volume as a function of TOC contents for each sorption process as shown in equation (13).

$$V_{L,ads}(TOC, T) = 3.0199 + 0.9240 \times TOC - 0.0027 \times T \times (TOC + 3.00) \quad (13a)$$

$$V_{L,des}(TOC, T) = 2.2093 + 0.6861 \times TOC - 0.0030 \times T \times (TOC + 2.79) \quad (13b)$$

Similar equations were also developed for the Langmuir volume as a function of COC as shown in equation (14).

$$V_{L,ads}(COC, T) = 6.5456 + 0.0144 \times COC - 6.7 \times 10^{-5} \times T \times (COC - 438.4) \quad (14a)$$

$$V_{L,des}(COC, T) = 4.5215 + 0.0104 \times COC - 5.2 \times 10^{-5} \times T \times (COC - 358.5) \quad (14b)$$

Fig. 12 shows example plots of actual and calculated Langmuir volumes for adsorption and desorption isotherms respectively using both the TOC-based and the COC-based models. The results showed that both models can adequately reproduce the actual Langmuir volumes with acceptable errors. Figures A6 and A7 (appendix A) contain the comparison plots for actual and predicted Langmuir volumes at all test temperatures.

Fig. 13 shows a comparison of the relative errors associated with the TOC-based and the COC-based models for the adsorption isotherms at each test temperature. The errors are of similar magnitudes indicating the reliability of using COC as a single predictor to account for the effect of clay contents in this Formation.

Also, Fig. 11(d) (and Figure A5) shows that a linear relationship exists between Langmuir pressure and Langmuir volume for both sorption processes. If the slope and vertical intercept of the straight-line trend between  $P_L$  and  $V_L$  are  $m_1$  and  $c_1$  respectively, then:

$$P_L = m_1 \times V_L + c_1 \quad (15)$$

It was also observed that the slopes and intercepts of the lines in Figure A5 are quadratic functions of temperature. Therefore, for temperature  $T$  in °C, the temperature-dependence of  $m_1$  and  $c_1$  in Eqn. (15) can be represented by the following equations:

$$m_1(T) = a_0 T^2 + a_1 T + a_2 \quad (16)$$

$$c_1(T) = b_0 T^2 + b_1 T + b_2 \quad (17)$$

The values of the coefficients  $a_i$  and  $b_i$  ( $i = 0, 1, 2$ ) in equations (16) and (17) are summarised in Table 6.

Fig. 14 shows examples comparing the predicted Langmuir pressures for adsorption and desorption isotherms respectively with the corresponding actual values. Again, the model's predictions adequately match the actual values. Figures A8 and A9 (appendix A) contain the comparison plots for actual and predicted Langmuir pressures at all test temperatures.

While the analytical models developed here for Langmuir parameters as functions of temperature and rock properties show good performances in predicting experimental values, they should be used with

caution considering the assumptions underlying their development. The following assumptions made in their developments may limit their performances to new datasets:

1. The isotherms were characterised by early pore saturation and could only be modelled using a "hybrid" approach.
2. The Langmuir parameters used in developing the models are highly-dependent on the value of adsorbed phase density calculated from D-R model.
3. The samples used in this work are clay-dominated, with TOC ranging from 0.28 to 4.16 wt%. The models' performances may deteriorate in high TOC samples (with low clay contents).
4. The models' performances may also deteriorate at higher temperatures where the excess adsorption isotherms might peak a little earlier resulting in lower adsorbed phase densities and poorer relationships between Langmuir parameters and TOC contents or COC.

## 5. Conclusions

This study presents the adsorption and desorption isotherms of methane on shale samples from the Ordovician Goldwyer Formation in the Canning Basin of Western Australia. The results showed that methane adsorption in these shales was characterised by early pore saturation resulting in peak excess adsorptions at about 5 MPa. Also, for all test temperatures, desorption isotherms were in hysteresis with the adsorption curves resulting in different temperature-dependent model parameters for both processes. Moreover, the size of the hysteresis loop was also affected negatively by temperature. Langmuir volumes for both processes strongly correlated positively with the TOC contents but showed weak to no significant relationship with the clay contents. However, the ratio of clay to organic carbon (COC), used to capture the combined effect of both TOC and clay contents, showed negative correlations with Langmuir volumes for both the adsorption and desorption processes. While the areal hysteresis index (AHI) and the improved hysteresis index (IHI) did not show any appreciable correlations with rock properties, the absolute values of the hysteresis area showed strong correlations with the TOC content and COC. Lastly, analytical models were developed for the temperature-dependence of Langmuir volume as function of TOC contents and COC for each sorption process. The models showed significant match with experimental results and as such, can be adopted for temperature conditions beyond those investigated in this study.

## Credit author statement

Jamiu M. Ekundayo: Conceptualization, Data curation, Formal analysis, Investigation, Methodology, Writing – original draft preparation. Reza Rezaee: Supervision, Funding acquisition, Writing – reviewing & editing. Chunyan Fan: Writing – reviewing & editing

## Data availability

All the data related to this article have been included in the manuscript, and associated appendix, either as tables or figures.

## Declaration of competing interest

The authors declare that they have no known competing financial interests or personal relationships that could have appeared to influence the work reported in this paper.

## Acknowledgments

This work is supported by open fund (PLN201902) of State Key Laboratory of Oil and Gas Reservoir Geology and Exploitation (Southwest Petroleum University). The authors would like to acknowledge the



contributions of Australian Government Research Training Program and Curtin Research Scholarships and the Unconventional Gas Research Group at the Discipline of Petroleum Engineering, Western Australian School of Mines: Minerals, Energy and Chemical Engineering in

supporting this research. The authors also acknowledge the support of Western Australia's Department of Mines, Industry Regulation and Safety and Finder Energy in providing the shale samples used in this study.

## Appendix A

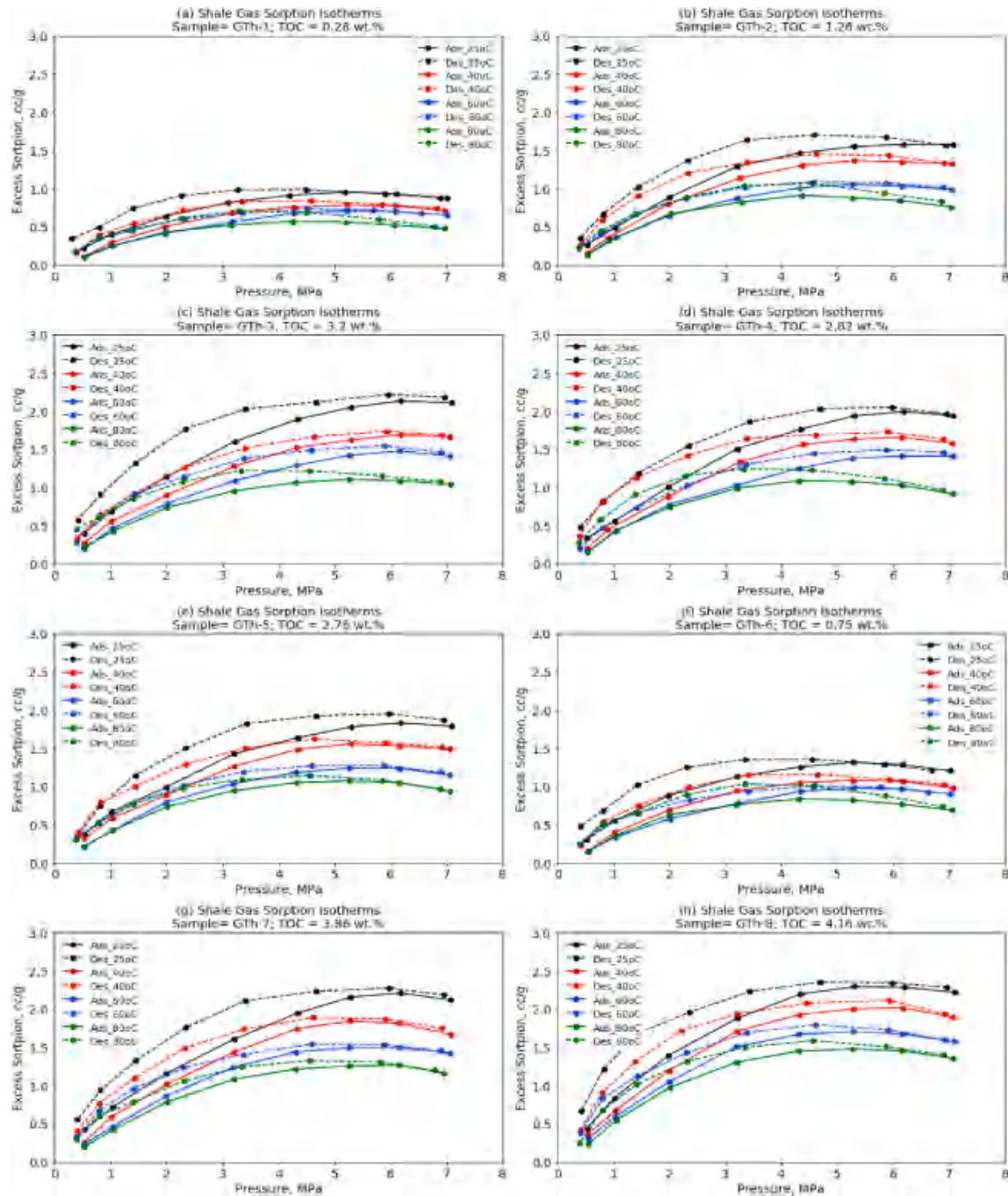


Figure A1. Shale gas adsorption and desorption isotherms and their associated hysteresis

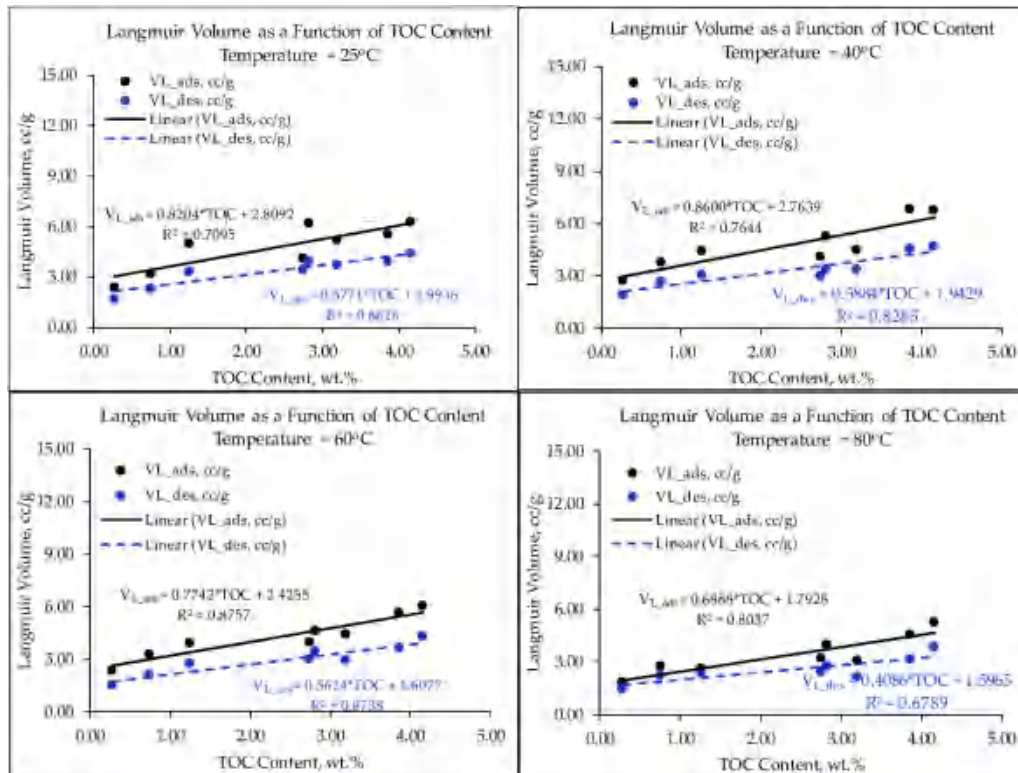


Figure A2. Relationship between Langmuir volumes and TOC contents for all test temperatures

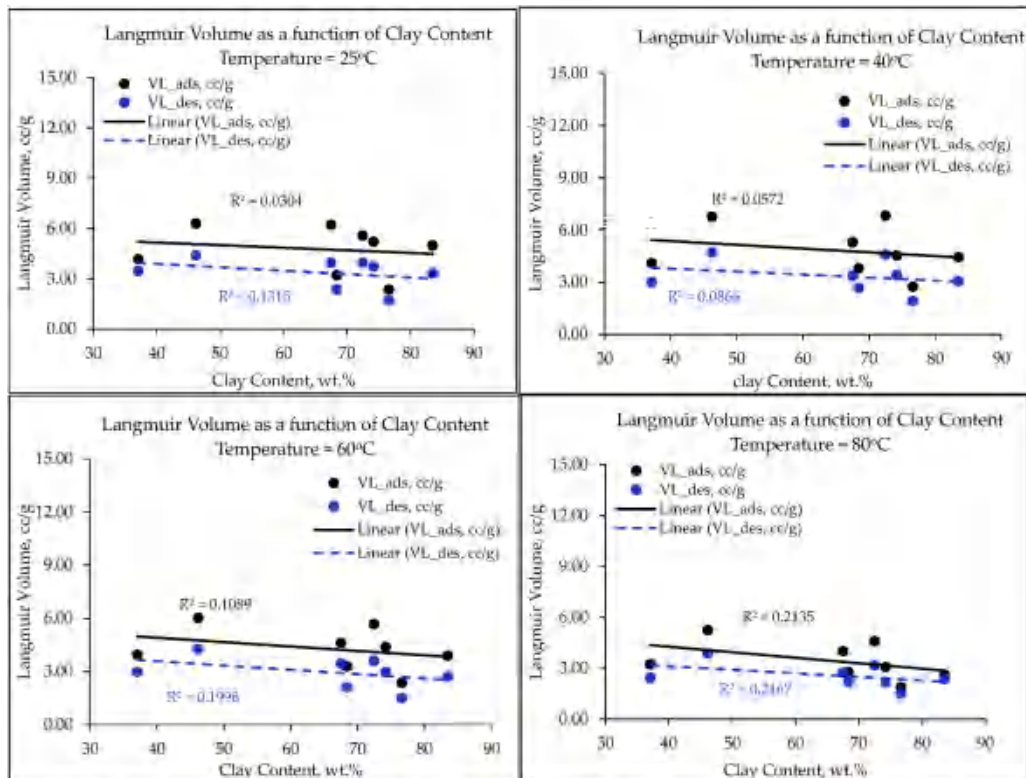


Figure A3. Relationship between Langmuir volumes and clay contents for all test temperatures

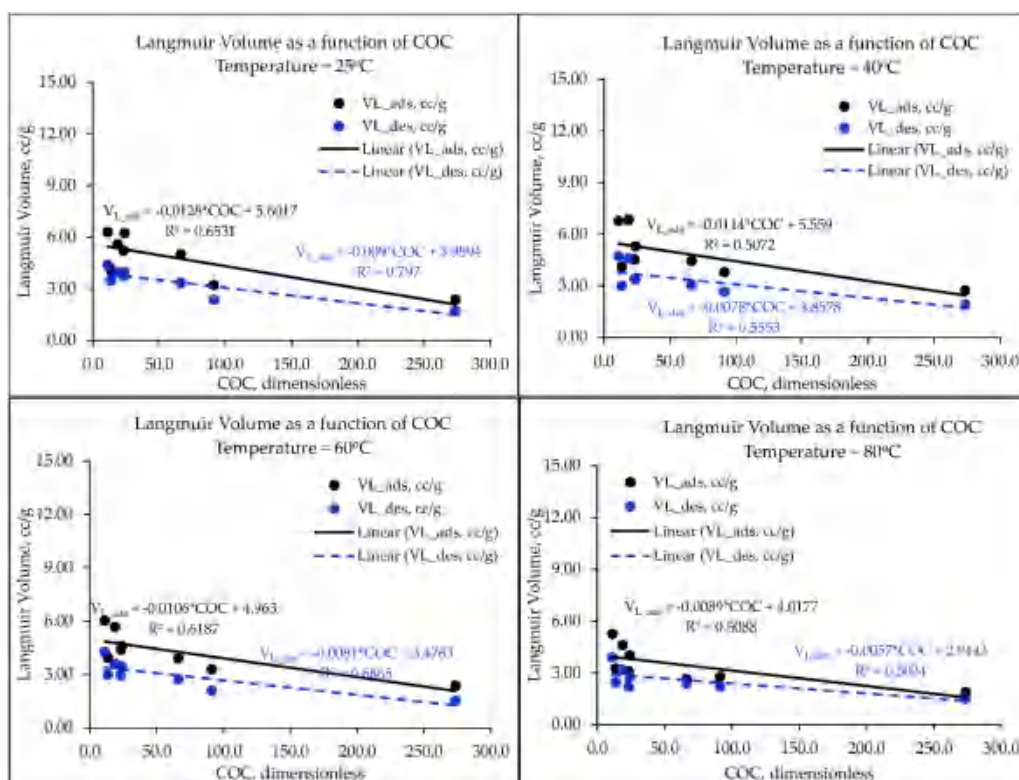


Figure A4. Relationship between Langmuir volumes and COC for all test temperatures

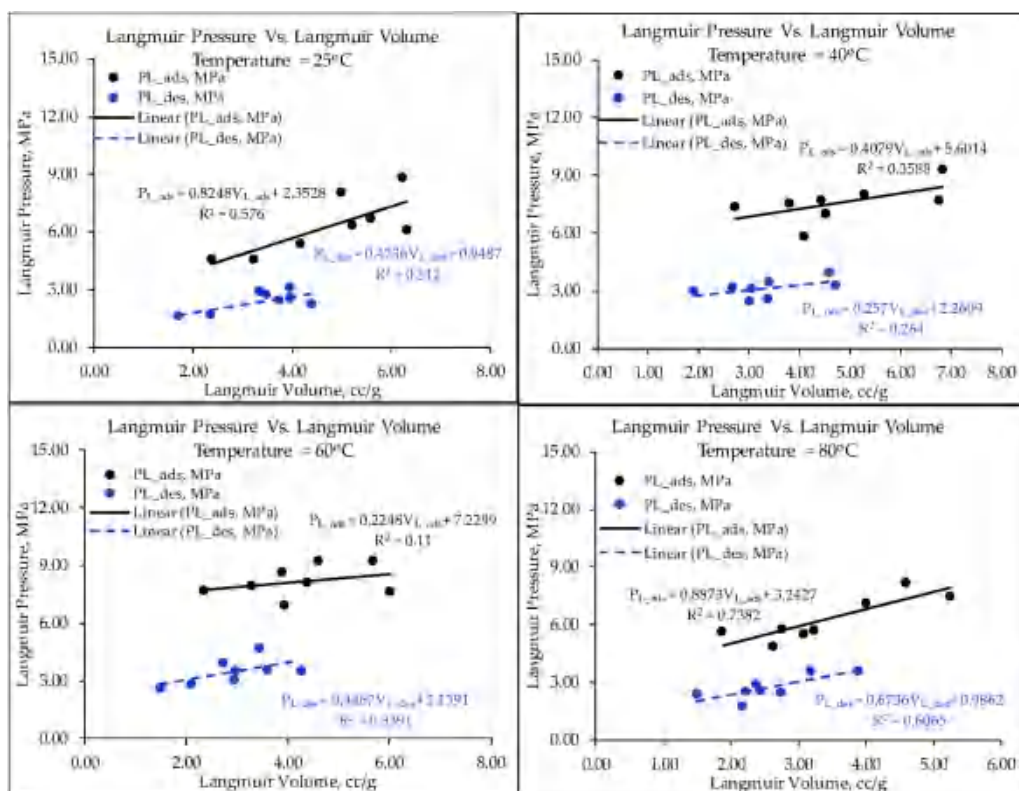


Figure A5. Relationship between Langmuir parameters for all test temperatures



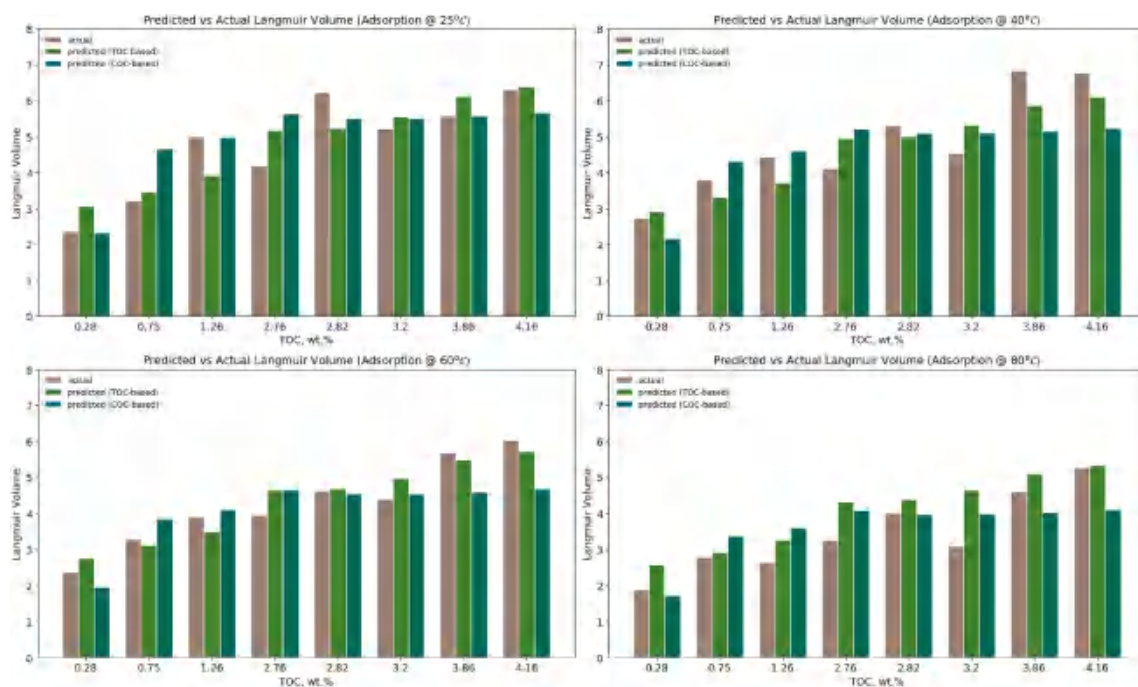


Figure A6. Comparing predicted and actual Langmuir volumes for adsorption isotherms

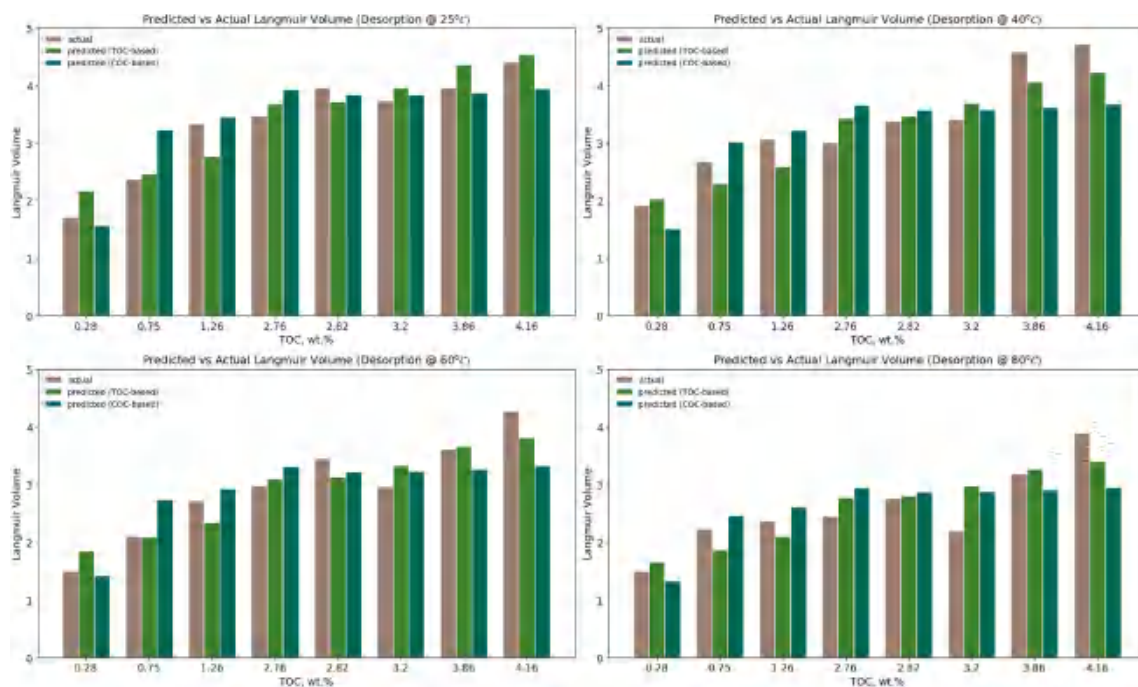


Figure A7. Comparing predicted and actual Langmuir volumes for desorption isotherms

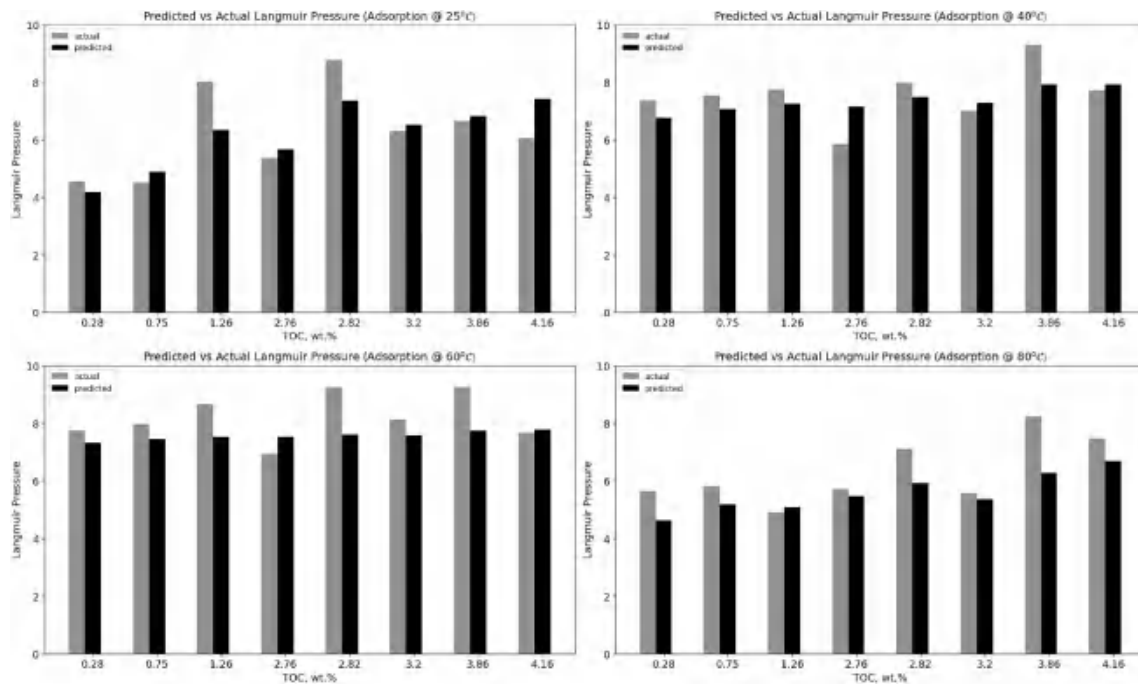


Figure A8. Comparing predicted and actual Langmuir pressures for adsorption isotherms

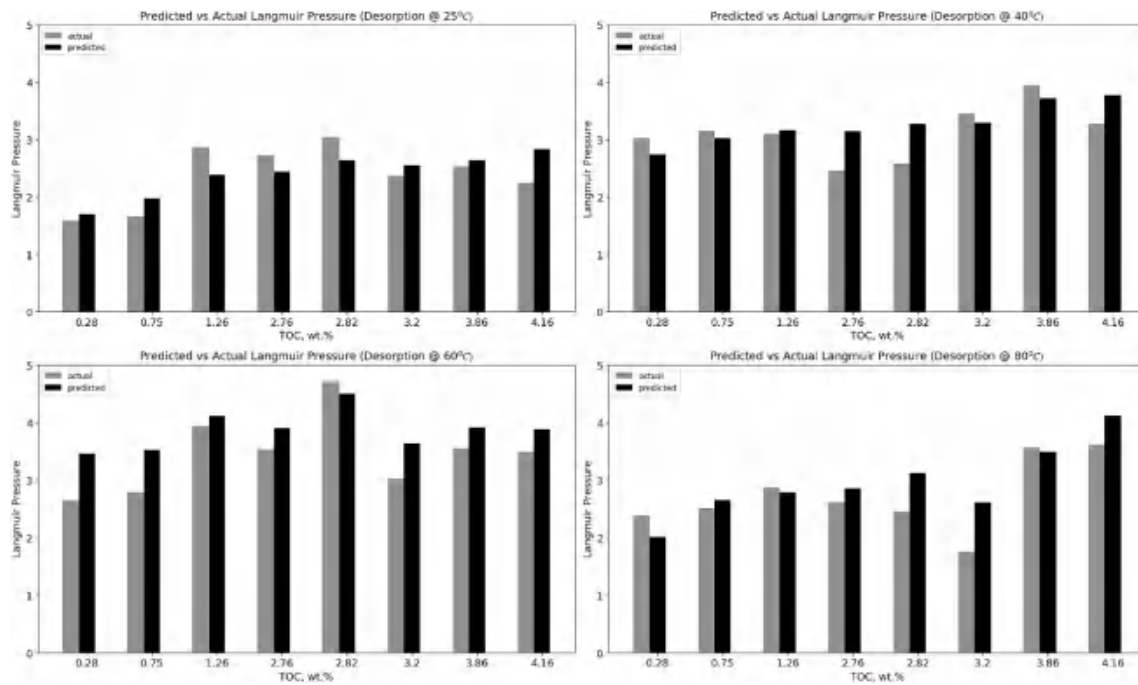


Figure A9. Comparing predicted and actual Langmuir pressures for adsorption isotherms

### Nomenclature and units

$AHI$	Areal Hysteresis Index
$D$	D-R's parameter related to pore structure, dimensionless
$E$	Characteristic energy of adsorption, $\text{Jmol}^{-1}$
$E_o$	Characteristic energy of adsorption of a reference vapour, $\text{Jmol}^{-1}$
$K$	Adsorption equilibrium constant, dimensionless
$P$	Pressure, MPa
$P_L$	Langmuir pressure, MPa
$P_{max}$	Maximum equilibrium pressure, MPa
$R$	Gas constant, $\text{Jmol}^{-1}\text{K}^{-1}$

$T$	Temperature, K
$V_{abs}$	Absolute adsorbed volume, cc/g
$V_{exc}$	Excess adsorbed volume, cc/g
$V_L$	Langmuir volume, cc/g
$V_o$	Maximum absolute adsorption (D-R model)
$\beta$	Similarity constant
$\rho_{ads}$	Adsorbed phase density, kg/m <sup>3</sup>
$\rho_{bulk}$	Bulk gas density, kg/m <sup>3</sup>
$\Delta G$	Gibb's free energy change, J/mol

## References

- Alshakhs, M., 2017. Shale Play Assessment of the Goldwyer Formation in the Canning Basin Using Property Modelling. Curtin University. MPhil.
- Amrhar, O., Nassali, H., Elyoubi, M.S., 2015. Two and three-parameter isothermal modeling for adsorption of Crystal Violet dye onto Natural Illitic Clay: nonlinear regression analysis. *J. Chem. Pharmaceut. Res.* 7 (9), 892–903.
- Bahar, M., Triche, N.E., 2013. Shale gas volumetrics of unconventional resource plays in the Canning Basin. In: Western Australia. Paper Presented at the SPE Unconventional Resources Conference and Exhibition-Asia Pacific. Australia, Brisbane. <https://doi.org/10.2118/167078-MS>.
- Battistutta, E., van Hemert, P., Lutynski, M., Bruining, H., Wolf, K.-H., 2010. Swelling and sorption experiments on methane, nitrogen and carbon dioxide on dry Selar Cornish coal. *Int. J. Coal Geol.* 84 (1), 39–48. <https://doi.org/10.1016/j.coal.2010.08.002>.
- Bell, G.J., Rakop, K.C., 1986. Hysteresis of methane/coal sorption isotherms. In: Paper Presented at the 61st SPE-ATCE, New Orleans, LA. <https://doi.org/10.2118/15454-MS>.
- Bhowmik, S., Dutta, P., 2019. A study on the effect of gas shale composition and pore structure on methane sorption. *J. Nat. Gas Sci. Eng.* 62, 144–156. <https://doi.org/10.1016/j.jngse.2018.12.009>.
- Brandani, S., Mangano, E., Sarkisov, L., 2016. Net, excess and absolute adsorption and adsorption of helium. *Adsorption* 22(2), 261–276. <https://doi.org/10.1007/s10450-016-9766-0>.
- Brunauer, S., Emmett, P.H., Teller, E., 1938. Adsorption of gases in multimolecular layers. *J. Am. Chem. Soc.* 60, 309–319. <https://doi.org/10.1021/ja01269a023>.
- Buckingham, A.D., Disch, R.L., Dunmur, D.A., 1968. Quadrupole moments of some simple molecules. *J. Am. Chem. Soc.* 90, 3104–3107. <https://doi.org/10.1021/ja01014a023>.
- Busch, A., Gensterblum, Y., Krooss, B.M., 2003. Methane and CO<sub>2</sub> sorption and desorption measurements on dry Argonne premium coals: pure components and mixtures. *Int. J. Coal Geol.* 55 (2), 205–224. [https://doi.org/10.1016/S0166-5162\(03\)00113-7](https://doi.org/10.1016/S0166-5162(03)00113-7).
- Cadman, S.J., Pain, L., Vuckovic, V., le Poidevin, S.R., 1993. Canning Basin. (Report 9). Western Australia: W.A. Bureau of Resource Sciences.
- Coasne, B., Galarneau, A., Di Renzo, F., Pellenq, R.J.M., 2010. Molecular simulation of nitrogen adsorption in nanoporous silica. *Langmuir* 26 (13), 10872–10881. <https://doi.org/10.1021/la100757b>.
- Cui, X., Bustin, R.M., Chikatarla, L., 2007. Adsorption-induced coal swelling and stress: implications for methane production and acid gas sequestration into coal seams. *J. Geophys. Res.: Solid Earth* 112 (B10). <https://doi.org/10.1029/2004JB003482>.
- Curtis, J.B., 2002. Fractured shale-gas systems. *AAPG (Am. Assoc. Pet. Geol.) Bull.* 86 (11), 1921–1938. <https://doi.org/10.1306/61EEDDBE-173E-11D7-8645000102C1865D>.
- Delle Piane, C., Almqvist, B.S.G., MacRae, C.M., Torpy, A., Mory, A.J., Dewhurst, D.N., 2015. Texture and diagenesis of Ordovician shale from the Canning Basin, Western Australia: implications for elastic anisotropy and geomechanical properties. *Mar. Petrol. Geol.* 59, 56–71. <https://doi.org/10.1016/j.marpetgeo.2014.07.017>.
- Do, D.D., Do, H.D., 2005. Adsorption of argon from sub- to supercritical conditions on graphitized thermal carbon black and in graphitic slit pores: a grand canonical Monte Carlo simulation study. *J. Chem. Phys.* 123 (8), 84701. <https://doi.org/10.1063/1.1996573>.
- Dutta, P., Bhowmik, S., Das, S., 2011. Methane and carbon dioxide sorption on a set of coals from India. *Int. J. Coal Geol.* 85 (3), 289–299. <https://doi.org/10.1016/j.coal.2010.12.004>.
- Ekundayo, J., Rezaee, R., 2019a. Effect of equation of states on high pressure volumetric measurements of methane-coal sorption isotherms - Part 1: volumes of free space and methane adsorption isotherms. *Energy & fuels*. <https://doi.org/10.1021/acs.energyfuels.8b04016>.
- Ekundayo, J.M., Rezaee, R., Fan, C., 2020. Effects of gas sorption hysteresis on gas production from organic-rich gas shale reservoirs. Paper presented at the SPE asia pacific oil & gas conference and exhibition (SPE APOGCE) 2020, virtual (accepted manuscript). <https://doi.org/10.2118/202462-MS>.
- Ekundayo, M.J., Rezaee, R., 2019b. Numerical simulation of gas production from gas shale reservoirs-influence of gas sorption hysteresis. *Energies* 12 (18), 1–12. <https://doi.org/10.3390/en12183405>.
- Ekundayo, M.J., Rezaee, R., 2019c. Volumetric measurements of methane-coal adsorption and desorption isotherms—effects of equations of state and implication for initial gas reserves. *Energies* 12 (10). <https://doi.org/10.3390/en12102022>.
- Feng, Y.-Y., Yang, W., Chu, W., 2016. Coalbed methane adsorption and desorption characteristics related to coal particle size. *Chin. Phys. B* 25 (6), 68102. <https://doi.org/10.1088/1674-1056/25/6/068102>.
- Fertl, W.H., Chilingar, G.V., 1988. Total organic carbon content determined from well logs. *SPE Form. Eval.* 3 (2), 407–419. <https://doi.org/10.2118/15612-PA>.
- Gasparik, M., Ghanizadeh, A., Bertier, P., Gensterblum, Y., Bouw, S., Krooss, B.M., 2012. High-pressure methane sorption isotherms of black shales from The Netherlands. *Energy Fuel.* 26, 4995–5004. <https://doi.org/10.1021/ef300405g>.
- Goodman, A.L., Busch, A., Duffy, G.J., Fitzgerald, J.E., Gasem, K.A.M., Gensterblum, Y., Krooss, B.M., Levy, J., Ozdemir, E., Pan, Z., Robinson, R.L., Schroeder, K., Sudibandriyo, M., White, C.M., 2004. An inter-laboratory comparison of CO<sub>2</sub> isotherms measured on argonne premium coal samples. *Energy Fuel.* 18 (4), 1175–1182. <https://doi.org/10.1021/ef034104h>.
- Guo, X., Qin, Z., Yang, R., Dong, T., He, S., Hao, F., Yi, J., Shu, Z., Bao, H., Liu, K., 2019. Comparison of pore systems of clay-rich and silica-rich gas shales in the lower Silurian Longmaxi formation from the Jiaoshiba area in the eastern Sichuan Basin, China. *Mar. Petrol. Geol.* 101, 265–280. <https://doi.org/10.1016/j.marpetgeo.2018.11.038>.
- Haines, P., 2004. Depositional facies and regional correlations of the ordovician goldwyer and nita formations, Canning Basin, western Australia, with implications for petroleum exploration. *Geol. Survey Western Australia, record*, 7.
- Hashimoto, T., Bailey, A.H.E., Chirinos, A., Carr, L.K., 2018. Onshore Basin Inventory Volume 2: the Canning, Perth and Officer Basins. Geoscience Australia, Canberra.
- Hutson, N.D., Yang, R.T., 1997. Theoretical basis for the Dubinin-Radushkevitch (D-R) adsorption isotherm equation. *Adsorption* 3 (3), 189–195. <https://doi.org/10.1007/BF01650130>.
- Jessen, K., Tang, G.-Q., Kovscek, A.R., 2008. Laboratory and simulation investigation of enhanced coalbed methane recovery by gas injection. *Transport Porous Media* 73 (2), 141–159. <https://doi.org/10.1007/s11242-007-9165-9>.
- Johnson, L., Smith, G., Rezaee, R., Kaddhodaie, A., 2019. A 3D model of the unconventional play in the Goldwyer Formation: an integrated shale rock characterisation over the Broome Platform, Canning Basin. In: Paper Presented at the Asia Pacific Unconventional Resources Technology Conference. Australia, Brisbane. <https://doi.org/10.15530/AP-URTEC-2019-19831210.15530/AP-URTEC-2019-198312>.
- Johnson, L.M., 2019. Integrated Reservoir Characterization of the Goldwyer Formation. Canning Basin. (PhD). Curtin University, Curtin University. Retrieved from. <http://hdl.handle.net/20.500.11937/77189>.
- Jun-yi, L., Zheng-song, Q., Wei-an, H., Yang, L., Ding-ding, S., 2014. Nano-pore structure characterization of shales using gas adsorption and mercury intrusion techniques. *J. Chem. Pharmaceut. Res.* 6 (4), 850–857.
- Kennard, J.M., Jackson, M.J., Romine, K.K., Shaw, R.D., Southgate, P.N., 1994. Depositional sequences and associated petroleum systems of the Canning Basin, WA. In: Purcell, P.G., Purcell, R.R. (Eds.), *The Sedimentary Basins of Western Australia*. Petroleum Exploration Society of Australia Symposium, Perth, pp. 657–676.
- Kierlik, E., Monson, P.A., Rosinberg, M.L., Tarjus, G., 2002. Adsorption hysteresis and capillary condensation in disordered porous solids: a density functional study. *J. Phys. Condens. Matter* 14, 9295–9315. <https://doi.org/10.1088/0953-8984/14/40/319>.
- King, G.R., 1993. Material-balance techniques for coal-seam and devonian shale gas reservoirs with limited water influx. *SPE Reservoir Eng.* 8 (1), 67–72. <https://doi.org/10.2118/20730-PA>.
- Lafarge, E., Marquis, F., Pillot, D., 1998. Rock-eval 6 applications in hydrocarbon exploration, production, and soil contamination studies. *Rev. Inst. Fr. Petrol* 53 (4), 421–437. <https://doi.org/10.2516/ogst:1998036>.
- Langmuir, I., 1918. The adsorption of gases on plane surfaces of glass, mica and platinum. *J. Am. Chem. Soc.* 40 (9), 1361–1403. <https://doi.org/10.1021/ja02242a004>.
- Lastoskie, C., Gubbins, K.E., Quirke, N., 1993. Pore size distribution analysis of microporous carbons: a density functional theory approach. *J. Phys. Chem.* 97 (18), 4786–4796. <https://doi.org/10.1021/j100120a035>.
- Lastoskie, C.M., Quirke, N., Gubbins, K.E., 1997. Chapter 15. Structure of porous adsorbents: analysis using density functional theory and molecular simulation. *Stud. Surf. Sci. Catal.* 104, 745–775. [https://doi.org/10.1016/S0167-2991\(97\)80078-X](https://doi.org/10.1016/S0167-2991(97)80078-X).
- Liu, Y.C., Chen, D.X., Qiu, N.S., Wang, Y., Fu, J., Huyan, Y., Jia, J.K., Wu, H., 2017a. Reservoir characteristics and methane adsorption capacity of the Upper Triassic continental shale in Western Sichuan Depression, China. *Aust. J. Earth Sci.* 64 (6), 807–823. <https://doi.org/10.1080/08120099.2017.1342174>.
- Liu, Z., He, Y., Xu, J., Huang, P., Jilani, G., 2008. The ratio of clay content to total organic carbon content is a useful parameter to predict adsorption of the herbicide butachlor



- in soils. *Environ. Pollut.* 152 (1), 163–171. <https://doi.org/10.1016/j.envpol.2007.05.006>, 1987.
- Liu, Z., Zhang, Z., Lu, Y., Ki Choi, S., Liu, X., 2017b. Sorption hysteresis characterization of CH<sub>4</sub> and CO<sub>2</sub> on anthracite, bituminous coal, and lignite at low pressure. *J. Energy Resour. Technol.* 140 (1) <https://doi.org/10.1115/1.4037483>, 012203–012203-012209.
- Ma, C., Dong, C., Lin, C., Elsworth, D., Luan, G., Sun, X., Liu, X., 2019. Influencing factors and fracability of lacustrine shale oil reservoirs. *Mar. Petrol. Geol.* 110, 463–471. <https://doi.org/10.1016/j.marpetgeo.2019.07.002>.
- Monson, G., 1983. A model of adsorption-desorption hysteresis in which hysteresis is primarily developed by the interconnections in a network of pores. *Proceed. Roy. Soc. Londn. Ser. A, Math. Phys. Sci.* 390, 47–72. <https://doi.org/10.1098/rspa.1983.0122>.
- Myers, A.L., Monson, P.A., 2002. Adsorption in porous materials at high Pressure: theory and experiment. *Langmuir* 18 (26), 10261–10273. <https://doi.org/10.1021/la026399h>.
- Myers, A.L., Monson, P.A., 2014. Physical adsorption of gases: the case for absolute adsorption as the basis for thermodynamic analysis. *Adsorption* 20 (4), 591–622. <https://doi.org/10.1007/s10450-014-9604-1>.
- Ozdemir, E., 2004. Chemistry of the Adsorption of Carbon Dioxide by Argonne Premium Coals and a Model to Simulate CO<sub>2</sub> Sequestration in Coal Seams. (Doctor of Philosophy). University of Pittsburgh, Unpublished. Retrieved from: <http://d-scholarship.pitt.edu/id/eprint/8142>.
- Ozdemir, E., 2017. Dynamic nature of supercritical CO<sub>2</sub> adsorption on coals. *Adsorption* 23 (1), 25–36. <https://doi.org/10.1007/s10450-016-9814-9>.
- Parra-Garcia, M., Sanchez, G., Dentith, M., George, A., 2014. Regional Structural and Stratigraphic Study of the Canning Basin, Western Australia, vol. 140. Department of Mines and Petroleum Government of Western Australia, Perth.
- Peters, K., Cassa, M., 1994. Applied source rock geochemistry. In: Magoon, L.B., Dow, W. G. (Eds.), AAPG Memoir, vol. 60. AAPG.
- Peters, K.E., 1986. Guidelines for evaluating petroleum source rock using programmed pyrolysis. Paper presented at the American chemical society. Sympos. Org. Geochem. Humic Subst. Kerogen and Coal, Philadelphia, Pennsylvania.
- Pevear, D.R., 1999. Illite and Hydrocarbon Exploration. Paper Presented at the National Academy of Sciences Colloquium “Geology, Mineralogy, and Human Welfare”, Irvine, CA.
- Rani, S., Sud, D., 2015. Effect of temperature on adsorption-desorption behaviour of triazophos in Indian soils. *Plant Soil Environ.* 61 (1), 36–42. [10.17221/704/2014-PSE](https://doi.org/10.17221/704/2014-PSE).
- Rexer, T.F.T., Benham, M.J., Aplin, A.C., Thomas, K.M., 2013. Methane adsorption on shale under simulated geological temperature and pressure conditions. *Energy Fuel* 27 (6), 3099–3109. <https://doi.org/10.1021/ef400381v>.
- Sakurovs, R., Day, S., Weir, S., Duffy, G., 2007. Application of a modified Dubinin–Radushkevich equation to adsorption of gases by coals under supercritical conditions. *Energy Fuel* 21 (2), 992–997. <https://doi.org/10.1021/ef0600614>.
- Soave, G.S., 1999. An effective modification of the Benedict-Webb-Rubin equation of state. *Fluid Phase Equil.* 164, 157–172. [https://doi.org/10.1016/S0378-3812\(99\)00252-6](https://doi.org/10.1016/S0378-3812(99)00252-6).
- Spaak, G., Edwards, D.S., Foster, C.B., Pagès, A., Summons, R.E., Sherwood, N., Grice, K., 2017. Environmental conditions and microbial community structure during the great ordovician biodiversification event; a multi-disciplinary study from the Canning Basin, western Australia. *Global Planet. Change* 159, 93–112. [10.1016/j.gloplacha.2017.10.010](https://doi.org/10.1016/j.gloplacha.2017.10.010).
- Taghavinejad, A., Sharifi, M., Heidaryan, E., Liu, K., Ostadhasan, M., 2020. Flow modeling in shale gas reservoirs: a comprehensive review. *J. Nat. Gas Sci. Eng.* 83, 103535. <https://doi.org/10.1016/j.jngse.2020.103535>.
- Tang, X., Ripepi, N., Luxbacher, K., Pitcher, E., 2017. Adsorption models for methane in shales: review, comparison, and application. *Energy Fuel* 31 (10), 10787–10801. <https://doi.org/10.1021/acs.energyfuels.7b01948>.
- Thommes, M., Kanero, K., Neimark, A.V., Olivier, J.P., Rodriguez-Reinoso, F., Rouquerol, J., Sing, K.S.W., 2015. Physisorption of gases, with special reference to the evaluation of surface area and pore size distribution (IUPAC technical Report). *Pure Appl. Chem.* 87 (9–10), 1051–1069. <https://doi.org/10.1515/pac-2014-1117>.
- Thompson, A., Goyne, K.W., 2012. Introduction to the sorption of chemical constituents in soils. *Nat. Edu. Knowledge* 4 (4), 7–11.
- Ustinov, E.A., Do, D.D., 2004. Application of density functional theory to capillary phenomena in cylindrical mesopores with radial and longitudinal density distributions. *J. Chem. Phys.* 120 (20), 9769–9781. <https://doi.org/10.1063/1.1710860>.
- Ustinov, E.A., Do, D.D., 2005. Modeling of adsorption in finite cylindrical pores by means of density functional theory. *Adsorption* 11, 455–477. <https://doi.org/10.1007/s10450-005-5606-3>.
- Wang, G., Ren, T., Zhang, L., Shu, L., 2017a. Undesorbable residual gas in coal seams and its influence on gas drainage. *Int. J. Min. Sci. Technol.* 27 (5), 763–769. <https://doi.org/10.1016/j.ijmst.2017.07.019>.
- Wang, J., Dong, M., Yang, Z., Gong, H., Li, Y., 2017b. Investigation of methane desorption and its effect on the gas production process from shale: experimental and mathematical study. *Energy Fuel* 31 (1), 205–216. <https://doi.org/10.1021/acs.energyfuels.6b02033>.
- Wang, K., Wang, G., Ren, T., Cheng, Y., 2014. Methane and CO<sub>2</sub> sorption hysteresis on coal: a critical review. *Int. J. Coal Geol.* 132, 60–80. <https://doi.org/10.1016/j.coal.2014.08.004>.
- Wei, G., Hu, Z., Zhang, X., Yu, R., Wang, L., 2017. Shale gas adsorption and desorption characteristics and its effects on shale permeability. *Energy Explor. Exploit.* 35 (4), 463–481. <https://doi.org/10.1177/0144598716684306>.
- Wei, G., Xiong, W., Gao, S., Hu, Z., Liu, H., Yu, R., 2013. Impact of temperature on the isothermal adsorption/desorption characteristics of shale gas. *Petrol. Explor. Dev.* 40 (4), 514–519. <https://doi.org/10.1177/0144598716684306>.
- Weishauptová, Z., Příbýl, O., Šýkorová, I., Machovič, V., 2015. Effect of bituminous coal properties on carbon dioxide and methane high pressure sorption. *Fuel* 139, 115–124. <https://doi.org/10.1016/j.fuel.2014.08.030>.
- Yan-Yan, F., Wen, Y., Wei, C., 2016. Coalbed methane adsorption and desorption characteristics related to coal particle size. *Chin. Phys. B* 25 (6).
- Yang, Y., Liu, S., 2020. Review of shale gas sorption and its models. *Energy Fuel*. <https://doi.org/10.1021/acs.energyfuels.0c02906>.
- Yuan, Y., Rezaee, R., Al-Khdeewi, E.A., Hu, S.-Y., Verrall, M., Zou, J., Liu, K., 2019. Impact of composition on pore structure properties in shale: implications for micro-/mesopore volume and surface area prediction. *Energy Fuel* 33 (10), 9619–9628. <https://doi.org/10.1021/acs.energyfuels.9b02232>.
- Zhang, J., Clennell, M.B., Liu, K., Pervukhina, M., Chen, G., Dewhurst, D.N., 2016. Methane and carbon dioxide adsorption on illite. *Energy Fuel* 30 (12), 10643–10652. <https://doi.org/10.1021/acs.energyfuels.6b01776>.
- Zhang, R., Liu, S., 2016. Experimental and theoretical characterization of methane and CO<sub>2</sub> sorption hysteresis in coals based on Langmuir desorption. *Int. J. Coal Geol.* 171, 49–60. <https://doi.org/10.1016/j.coal.2016.12.007>.
- Zhang, Y., Xing, W., Liu, S., Liu, Y., Yang, M., Zhao, J., Song, Y., 2015. Pure methane, carbon dioxide, and nitrogen adsorption on anthracite from China over a wide range of pressures and temperatures: experiments and modeling. *RSC Adv.* 5 (65), 52612–52623. [10.1039/C5RA05745K](https://doi.org/10.1039/C5RA05745K).
- Zhen, Y.Y., Normore, L.S., Dent, L.M., Percival, I.G., 2020. Middle ordovician (darriwilian) conodonts from the Goldwyer Formation of the Canning Basin, western Australia. *Alcheringa* 44 (1), 25–55. <https://doi.org/10.1080/03115518.2019.1618915>.
- Zhou, S., Xue, H., Ning, Y., Guo, W., Zhang, Q., 2018. Experimental study of supercritical methane adsorption in Longmaxi shale: insights into the density of adsorbed methane. *Fuel* 211, 140–148. <https://doi.org/10.1016/j.fuel.2017.09.065>.
- Zhu, H., Selim, H.M., 2000. Hysteretic behavior of metolachlor adsorption-desorption in soils. *Soil Sci.* 165 (8), 632–645. <https://doi.org/10.1097/00010694-200008000-00005>.
- Zou, J., Rezaee, R., 2016. Effect of particle size on high-pressure methane adsorption of coal. *Petrol. Res.* 1 (1), 53–58. [https://doi.org/10.1016/s2096-2495\(17\)30030-3](https://doi.org/10.1016/s2096-2495(17)30030-3).
- Zou, J., Rezaee, R., 2019. A prediction model for methane adsorption capacity in shale gas reservoirs. *Energies* 12 (280). <https://doi.org/10.3390/en12020280>.
- Zou, J., Rezaee, R., Liu, K., 2017. Effect of temperature on methane adsorption in shale gas reservoirs. *Energy Fuel* 31, 12081–12092. <https://doi.org/10.1021/acs.energyfuels.7b02639>.